

Mutual Information Based Pilot Design for ISAC

Ahmad Bazzi, Marwa Chafii

Abstract—The following paper presents a novel orthogonal pilot design dedicated for integrated sensing and communications (ISAC) systems performing multi-user communications and target detection. After careful characterization of both sensing and communication metrics based on mutual information (MI), we propose a multi-objective optimization problem (MOOP) tailored for pilot design, dedicated for simultaneously maximizing both sensing and communication MIs. Moreover, the MOOP is further simplified to a single-objective optimization problem, which characterizes trade-offs between sensing and communication performances. Due to the non-convex nature of the optimization problem, we propose to solve it via the projected gradient descent method on the Stiefel manifold. Closed-form gradient expressions are derived, which enable execution of the projected gradient descent algorithm. Furthermore, we prove convergence to a fixed orthogonal pilot matrix. Finally, we demonstrate the capabilities and superiority of the proposed pilot design, and corroborate relevant trade-offs between sensing MI and communication MI. In particular, significant signal-to-noise ratio (SNR) gains for communication are reported, while re-using the same pilots for target detection with significant gains in terms of probability of detection for fixed false-alarm probability. Other interesting findings are reported through simulations, such as an *information overlap* phenomenon, whereby the fruitful ISAC integration can be fully exploited.

Index Terms—Integrated sensing and communication (ISAC), dual-functional radar and communication, pilot design, performance tradeoff, information overlap, non-convex optimization, joint communication and sensing, Stiefel manifold

I. INTRODUCTION

To address the spectrum constraint resulting from the growing demand of wireless devices, integrated sensing and communication (ISAC) systems [1]–[5] have recently emerged as a key enabler to solve the ever-growing spectrum congestion problem, thus attracting both the interest of academia and industry. ISAC is currently presented as one strategy to reducing this problem by co-designing wireless communication functions and radar sensing on a single hardware platform and sharing the spectrum of both radar and communication systems, thus improving band-utilization efficiency. Therefore, radar sensing and communication tasks are carried out through a unified platform and a common radio waveform at the same time, over the same frequency band, utilizing the same antennas. It is worth noting that both sensing and communication have been treated as two separate fields since the 1900s. Then, radar waveforms performing communications have appeared, and vice-versa. For example, in 1967, pulse interval modulation was introduced to modulate communication data onto a pulse-based radar waveform, and orthogonal frequency-division multiplexing

(OFDM)-based sensing has been utilized to perform sensing with OFDM [6].

Earlier research efforts were dedicated towards spectrum co-existence, also referred to as radar-communication coexistence (RCC) [7]–[9], whereby both radar and communication co-exist at the price of deliberate interference caused by one sub-system onto the other. Therefore, interference cancellation methods have been designed to address the RCC interference issue, such as null space projection [10]. Unfortunately, allocating different frequency bands for these systems is neither practical nor sustainable, since both sensing and communication systems are requesting additional resources. Although being long thought of as two separate domains, sensing and communication are in fact, intimately entangled from an information-theoretic perspective [11]. To realize the goal of ISAC systems, however, various obstacles must be overcome. For example, this integration complicates the design of signal waveforms, resource and hardware allocation, and network operation. All of this motivates the search for innovative approaches to these issues in order to allow the advantages of the ISAC system in real-world deployments for sensing accuracy and high-rate communications.

The integration of sensing and communication into a unified system has opened up new possibilities for improving efficiency and enabling advanced applications. One critical avenue of research has been waveform design, where the goal is to develop waveforms capable of balancing the requirements of sensing and communication. For instance, waveforms have been tailored to minimize multi-user communication interference while preserving essential chirp characteristics with configurable peak-to-average power ratio (PAPR) [12]. In other cases, full-duplex waveform frameworks utilize the idle time of pulsed radar systems to enable seamless communication transmissions, ensuring efficient resource utilization [13]. Sparse vector coding techniques have also been explored to design waveforms with low sidelobes and guaranteed communication performance, addressing the challenges of coexisting functionalities [14]. As far as waveform sidelobe is concerned, it was recently proven [15] that the OFDM waveform achieves the lowest sidelobe level at *each lag* of the so-called periodic auto-correlation function for sub-Gaussian constellations, e.g. quadrature amplitude modulation (QAM) and phase shift keying (PSK) type constellations. On the other hand, it was also proven [15] that for super-Gaussian constellations single-carrier waveforms with cyclic prefix is the waveform that achieves the lowest sidelobes. Beyond waveform design, beamforming plays an important role in further enabling ISAC systems to achieve joint sensing and communication objectives. For example, an approach is to optimize beamforming matrices to reduce the outage signal to interference plus noise ratio (SINR) probability while

Ahmad Bazzi and Marwa Chafii is with Engineering Division, New York University (NYU) Abu Dhabi, 129188, UAE and NYU WIRELESS, NYU Tandon School of Engineering, Brooklyn, 11201, NY, USA (email: ahmad.bazzi@nyu.edu, marwa.chafii@nyu.edu).

maximizing radar output power in the Bartlett sense [16], which can promote ISAC applications when imperfect channel state information is known, due to some estimation errors. A weighted combination of the sum rate and the Cramér-Rao bound (CRB) was optimized for transmit beamforming design in [17], under an available transmit power budget. From interference management perspective, joint transmit and receive beamformers have proven effective in beyond 5G cellular internet of things scenarios, highlighting the interplay between interference mitigation and ISAC performance [18]. Further advancements integrate beamforming with dynamic elements such as unmanned aerial vehicle (UAV) trajectory planning to maximize system performance while adhering to beam pattern requirements [19]. In other instances, beamformers have been designed to optimize communication signal-to-noise ratio (SNR) while maintaining integrated sidelobe ratio guarantees for radar sensing [20]. Additionally, deep learning techniques have shown promise for tracking sensing parameters in vehicular networks, adding a layer of intelligence to ISAC operations [21]. Theoretical analysis have provided insights into the trade-offs and limitations of ISAC systems. Frameworks that assess detection and false-alarm probabilities offer valuable tools for performance evaluation [22], while other studies quantify trade-offs between CRB and communication capacity, offering a deeper understanding of ISAC system capabilities [11]. The evolution of ISAC is also being shaped by its integration with emerging technologies, including holographic multiple-input, multiple-output (MIMO) [23], massive MIMO [24], reconfigurable intelligent surface [25], simultaneously transmitting and reflecting surfaces [26], and OFDM [27]. These combinations extend the reach and applicability of ISAC, positioning it as a cornerstone for future wireless systems.

Nevertheless, most of the aforementioned designs focus only on waveform and beamforming designs targeting capacity, spectral efficiency, or sum-rate maximization without addressing channel estimation concerns in the context of ISAC. Therefore, we find it crucial to provide pilots, that are good for both channel estimation and target detection. To this end, this paper considers ISAC base station (BS) pilot design with flexible ISAC trade-offs, intended for downlink (DL) communication users, while listening to the backscattered echo of the transmitted pilot. Meanwhile, the users utilize the pilot for channel estimation, for equalization and decoding purposes. The design aims at maximizing mutual information, for both communication and sensing, on the Stiefel manifold in order to preserve the orthogonality constraint on the pilots. A design parameter is highlighted that trades off communication and sensing performances. Towards this ISAC design, we are faced with a non-convex optimization problem, which can be efficiently and reliably solved via an appropriate projected gradient descent algorithm. It is worth emphasizing that our results show that these pilots can be effectively utilized for channel estimation at the user's end, while the ISAC BS can exploit the echo of the same pilot to detect targets. To that purpose, we have summarized our main contributions below.

- **Unified mutual information (MI) metric for pilot**

design framework. We derive a unified MI metric that enable pilots to perform target detection, while reliably utilized for channel estimation tasks for multi-user communications. In particular, a sensing MI metric is proposed to optimize target detection performance, while a communication MI metric is proposed to aid with channel estimation tasks. In this regard, a multi-objective optimization problem (MOOP) is devised to unify the proposed MI metrics into an ISAC MI metric. Usually, ISAC waveforms are designed with the purpose of guaranteeing reliable communication under some constraints on sensing metrics. Unlike this approach, the proposed framework designs orthogonal pilot waveforms with the purpose of aiding the communication channel estimation, which we show in Section VI, has positive reverberation effects on the communication capacity. Moreover, the same pilots are also optimized for target detection.

- **Non-convex optimization via projected gradient descent.** Being confronted with a MOOP, we first scalarize the problem, which gives rise to single-objective, but non-convex optimization problem, which is to be solved over the Stiefel manifold. We derive a projected gradient descent algorithm tailored for ISAC orthogonal pilot waveforms.
- **Connections with existing sensing and communication metrics.** We show how the proposed MI-based metrics for both communications and sensing are connected with classical performance metrics. In particular, we show that the communication MI-based metric, although intended for channel estimation purposes, positively influences the worst-case channel capacity, which improves communication performance. Moreover, the proposed sensing MI-based metric is asymptotically connected to the detection probability of the most powerful detection test, according to Neyman-Pearson criterion, under a fixed false alarm probability.

Furthermore, we unveil some important insights, i.e.

- The number of transmit antennas and the number of pilot symbols have profound impact on the ISAC MI achievable tradeoffs, allowing a flexible design of pilots, even in the presence of clutter.
- The ISAC MI performance is influenced by the target location, where the closer the target approaches the mean of communication user angle of arrival (AoA), the pointier the Pareto frontier becomes. In particular, as the target approaches the communication user, the ISAC MI frontier is pushed outwards towards the utopia point. We term this phenomenon as the *information overlap* phenomenon, whereby the sensing and communication channels share common information. Consequently, using the same orthogonal pilot matrix, which is designed based on the proposed method, allows to simultaneously achieve better sensing and communication MI performance.
- The receiver operating characteristic (ROC) performance of an optimized orthogonal pilot matrix for communication is better than an non-optimized orthogonal pilot matrix. The ROC performance can be further improved

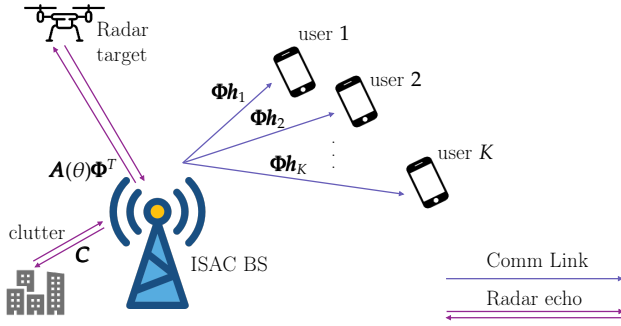


Fig. 1. ISAC scenario including an ISAC BS, an intended target with clutter and K communication users.

through a design parameter that controls the priority of sensing over communication.

- For multi-user communications, the symbol error rate (SER) performance utilizing the channel estimates aided by the generated pilot matrices exhibit gains as high as 1.6 dB for an SER level of 10^{-4} . This gain can be controlled through an ISAC design parameter trading off sensing for communications. Furthermore, SNR gains of about 6 dB are reported for normalized mean square error (NMSE) performance of channel estimation.
- For sake of completeness, we prove that the proposed projected gradient method approach can always converge to a stable pilot solution. In this regard, the convergence properties of the algorithm are derived.

The detailed structure of the following paper is given as follows. In Section II, we introduce the ISAC system model. Section III introduces mutual information metrics for the problem of pilot design, which enable us to optimize the pilots for both sensing and communication tasks. In Section IV, an optimization framework for ISAC pilot design is designed. Moreover, Section V describes a method to solve the pilot design problem in an iterative fashion, and its convergence property is described. Section VII provides numerical results to verify our analysis before concluding the paper in Section VIII. **Notation:** Upper-case and lower-case boldface letters denote matrices and vectors, respectively. $(\cdot)^T$, $(\cdot)^*$ and $(\cdot)^H$ represent the transpose, the conjugate and the transpose-conjugate operators. The statistical expectation is denoted as $\mathbb{E}[\cdot]$. The ℓ_2 norm of a vector \mathbf{x} is denoted as $\|\mathbf{x}\|$. The matrix \mathbf{I}_N is the identity matrix of size $N \times N$. The zero-vector is $\mathbf{0}$. For matrix indexing, the $(i, j)^{th}$ entry of matrix \mathbf{A} is denoted by $[\mathbf{A}]_{i,j}$ and its j^{th} column is denoted as $[\mathbf{A}]_{:,j}$. Also, vec is the vectorization operator, which vectorizes a matrix by stacking its columns, one on top of the other. The density $f_{\mathcal{CN}}(\mathbf{x}|\boldsymbol{\mu}, \boldsymbol{\Sigma})$ represents the probability density function of the complex Gaussian random variable \mathbf{x} following mean $\boldsymbol{\mu}$ and covariance $\boldsymbol{\Sigma}$.

II. SYSTEM MODEL

Consider an ISAC system composed of K single-antenna communication users, a radar target of interest, and a ISAC BS. Let the number of transmit and receive antennas at the BS be N_t and N_r , respectively. The communication users are considered to be located at arbitrary positions, whereas the target is supposed to be at a given angle θ_0 from the ISAC

BS. In the following, we describe the system model for both communication and radar sensing.

A. Communication Model

Consider the ISAC BS broadcasting a pilot signal in the DL sense over its N_t transmit antennas. In particular, let $\Phi \in \mathbb{C}^{L \times N_t}$ be the pilot matrix, to be designed, where $[\Phi]_{\ell,n}$ represents the ℓ^{th} pilot symbol transmitted over the n^{th} antenna. In matrix notation, we have

$$\Phi = [\Phi_1 \ \dots \ \Phi_L]^T. \quad (1)$$

Furthermore, let \mathbf{h}_k be the channel between ISAC BS and k^{th} communication user. Then, the received signal in the DL over L instances seen at the k^{th} communication user reads

$$\mathbf{y}_k = \Phi \mathbf{h}_k + \mathbf{n}_k. \quad (2)$$

This is the first stage of a communication system, commonly referred to as the training phase, where the goal is to reliably estimate $\mathbf{h}_1 \dots \mathbf{h}_K$. Note that no precoding is adopted and the goal here is to design Φ well-optimized for channel estimation, and target detection as will be described in Section III-B. In (2), $\mathbf{y}_k \in \mathbb{C}^{L \times 1}$ is the received signal vector at the k^{th} user and \mathbf{n}_k is background noise, assumed to be white Gaussian independently and identically distributed with zero mean, i.e. $\mathbf{n}_k \sim \mathcal{CN}(0, \sigma_k^2 \mathbf{I}_L)$.

We adopt the Gaussian mixture model (GMM) in order to model the communication channels between ISAC BS and the users. A GMM is a general model for multicasting, where each communication user is spatially distributed in a non-uniform geometric fashion. Even more, with a large number of mixtures, one can approximate any density with the aid of GMM [28], [29]. Typically, a GMM describes an ensemble of Gaussian distributions, whereby increasing the number of Gaussian components can contribute to better describing the channel [30]. The probability density function (PDF) of channel \mathbf{h}_m is modeled as GMM, i.e. a weighted sum of Gaussian densities as follows,

$$\phi_n(\mathbf{h}_k) = \sum_{n=1}^{N_k} \alpha_{k,n} \phi_n(\mathbf{h}_k), \quad (3)$$

where $\phi_n(\mathbf{h}_k) = f_{\mathcal{CN}}(\mathbf{h}_k|\boldsymbol{\mu}_{k,n}, \mathbf{R}_{k,n})$, where $\boldsymbol{\mu}_{k,n} \in \mathbb{C}^{N_t \times 1}$ and $\mathbf{R}_{k,n} \in \mathbb{C}^{N_t \times N_t}$. Furthermore, $\alpha_{k,n}$ are the so-called mixing coefficients, reflecting the probability that the n^{th} Gaussian component, i.e. $\phi_n(\mathbf{h}_k)$, is active in the (3), therefore, we must have $\sum_{n=1}^{N_k} \alpha_{k,n} = 1, \forall k$. Also, the number of Gaussian components modeling the k^{th} communication user is N_k . Finally, as indicated in [30], the set $\{\alpha_{k,n}, \boldsymbol{\mu}_{k,n}, \mathbf{R}_{k,n}\}_{n=1}^{N_k}$ are the GMM parameters that model channel component \mathbf{h}_k .

The communication users perform channel estimation, e.g. linear minimum mean square error (MMSE) estimation, and then feedback those estimates to the ISAC BS. The ISAC BS then uses those estimates to precode the modulated information as follows

$$\mathbf{Y}_c = \mathbf{H} \mathbf{W} \mathbf{S}_c + \mathbf{N}_c, \quad (4)$$

where $\mathbf{H} = [\mathbf{h}_1 \ \dots \ \mathbf{h}_K]^T$ is the communication channel matrix over all users, assumed fixed within a certain block. Moreover, $\mathbf{S}_c \in \mathbb{C}^{K \times B}$ belong to a certain constellation, e.g. 2^p -QAM and B is the block length. In addition, \mathbf{W} is a communication precoding matrix (e.g. zero-forcing (ZF) or MMSE precoding) that utilizes the channel estimates reported by the users. Equation 4 represents the second stage after

channel estimation, whereby \mathbf{W} is designed for precoding to maximize communication performance. In this paper, we have adopted the ZF precoding that makes use of the channel estimates given in the first stage.

B. Sensing Model

The radar sub-system within the ISAC BS system exploits the same pilot matrix as the one utilized for communication tasks, i.e. Φ . In precise, the pilots transmitted over N_t antennas and L slots are designed to satisfy both dual sensing and communication functionalities. Assuming a colocated monostatic MIMO radar setting, the received backscattered signal at the ISAC BS over N_r receiving antennas can be written as [31]

$$\mathbf{Y}_r = \gamma_0 \mathbf{a}_{N_r}(\theta_0) \mathbf{a}_{N_t}^T(\theta_0) \Phi^T + \sum_{i=1}^Q \gamma_i \mathbf{a}_{N_r}(\theta_i) \mathbf{a}_{N_t}^T(\theta_i) \Phi^T + \mathbf{Z}_r. \quad (5)$$

The AoAs and angle of departures (AoDs) are identical due to the monostatic sensing setting, i.e. the transmitter and receiver are assumed to very close, i.e. colocated. Indeed, due to geometric symmetry, the AoD, which measures the angle of the path departing from the ISAC BS towards the target/clutter is equal to the angle of the echo joining the same target/clutter back to the ISAC BS. This translates to identical AoAs and AoDs for both target and clutter. It is worth noting that this is not the case for bistatic sensing, however. The vectors $\mathbf{a}_{N_r}(\theta) \in \mathbb{C}^{N_r \times 1}$ and $\mathbf{a}_{N_t}(\theta) \in \mathbb{C}^{N_t \times 1}$ model the transmit/receive array steering vectors pointing towards angle θ , respectively. For instance, if a uniform linear antenna (ULA) array setting is adopted, then the steering vectors are given as follows

$$\mathbf{a}_{N_t}(\theta) = [1 \quad e^{j\frac{2\pi}{\lambda} d_t \sin(\theta)} \quad \dots \quad e^{j\frac{2\pi}{\lambda} d_t (N_t-1) \sin(\theta)}]^T, \quad (6)$$

$$\mathbf{a}_{N_r}(\theta) = [1 \quad e^{j\frac{2\pi}{\lambda} d_r \sin(\theta)} \quad \dots \quad e^{j\frac{2\pi}{\lambda} d_r (N_r-1) \sin(\theta)}]^T, \quad (7)$$

where λ is the wavelength and d_t, d_r are the inter-element spacing between transmit and receive antennas, respectively. Since a co-located setting is utilized, the AoD and AoA of the backscattered component is the same.

We assume that the above reception, sampling and signal processing happen within the same time interval referred to as the coherent processing interval (CPI) [20], [32], [33], which is an interval where $\theta_0, \theta_1 \dots \theta_Q$ and $\gamma_0, \gamma_1 \dots \gamma_Q$ remain unchanged [4]. The CPI length depends on the mobility of objects in the channels and is typically a few milliseconds when objects move at speeds of tens of meters per second. On the other hand, the γ_i 's vary between different realizations of \mathbf{Y}_r .¹ Therefore, following the Swerling-I model, we can assume that $\gamma_i \sim \mathcal{CN}(0, \nu_i)$ [34], [35]. In addition, the i^{th} clutter power is denoted as $\nu_i = \mathbb{E}[|\gamma_i|^2]$.

Furthermore, the backscattered signal $\mathbf{Y}_r \in \mathbb{C}^{N_r \times L}$ is the received radar vector and γ_0 is the complex channel gain of the reflected echo, containing two-way delay information between the ISAC BS and the radar target of interest. The angle θ represents the AoA of the target relative to the ISAC BS receive array. Nevertheless, due to clutter presence, the i^{th}

clutter source with complex gain γ_i is located at θ_i relative to the ISAC BS. In addition, Q is the number of clutter components in the environment. The noise of the radar sub-system is i.i.d Gaussian modeled as $\mathbf{Z}_r \sim \mathcal{N}(0, \sigma_r^2 \mathbf{I}_N)$. In the next section, we introduce performance metrics to optimize the pilot matrix intended for both sensing and communication tasks.

In this work, we assumed a clear line of sight (LoS) component between the target and the BS for the radar channel, for e.g. a flying UAV. This assumption aligns with scenarios where the BS senses highly visible targets, as noted in the 3rd Generation Partnership Project (3GPP) feasibility study on ISAC [36], which includes use cases like UAV trajectory tracking and detection. UAV targets typically exhibit a strong LoS channel, which differs significantly from the ground-based user communication channel. For the communication channel, the scenario is more complex due to effects like shadowing, multipath, and non line of sight (NLoS) conditions. These factors often lead to distributions such as Rician (via K -factor modeling) or Nakagami for severe fading. To address this variability, we adopted a GMM model, which is versatile for approximating unknown channel distributions. Even when the actual channel is not inherently a GMM, its flexibility allows it to approximate a wide range of distributions accurately [37]. Moreover, GMM models are particularly useful under the weakest assumptions about the channel, as they can represent any continuous probability distribution with arbitrary precision [38]. This makes them a robust choice for generalizing ISAC pilot design in uncertain communication channel conditions.

III. PERFORMANCE METRICS

Radar waveforms are designed to enhance various sensing capabilities, such as detection, imaging and location estimation accuracy. On the other hand, communication waveforms maximize the amount of information reliably transferred between the BS and the communication users. In this study, the aim is to design a common pilot matrix to simultaneously optimize the sensing detection potential at the ISAC BS and channel estimation reliability at all communication users. In this section, we attempt to unify the communication and sensing performance metrics via appropriate mutual information based indicators.

A. Mutual Information for Communications

The MI is a special instance of the more general quantity, that is the relative entropy, which measures the distance between probability distributions [39]. Following [39], the MI between the received DL signal at the k^{th} communication user and the k^{th} channel vector can be expressed as

$$I(\mathbf{y}_k; \mathbf{h}_k) = h(\mathbf{y}_k) - h(\mathbf{y}_k | \mathbf{h}_k), \quad (8)$$

where $h(\mathbf{y}_k)$ is the differential entropy of the received signal \mathbf{y}_k and $h(\mathbf{y}_k | \mathbf{h}_k)$ stands for differential entropy of $h(\mathbf{y}_k)$ given \mathbf{h}_k . In the following, we propose an MI-based metric associated with the k^{th} communication user.

Proposition 1: For a given pilot matrix Φ , the MI between \mathbf{y}_k and \mathbf{h}_k can be approximated as $I(\mathbf{y}_k; \mathbf{h}_k) \simeq \mathcal{M}_k^{\text{comm}}(\Phi)$ where

$$\mathcal{M}_k^{\text{comm}}(\Phi) \triangleq -\log \left(\sum_{n=1}^{N_k} \frac{\alpha_{k,n} e^{-\beta_{k,n}(\Phi)}}{\det(\Sigma_{k,n}(\Phi))} \right) + \text{cnst}, \quad (9)$$

¹This occurs when the ISAC BS attempts to transmit the same pilot matrix Φ within another frame.

and

$$\beta_{k,n}(\Phi) = \bar{\boldsymbol{\mu}}_{k,n}^H \Phi^H \Sigma_{k,n}^{-1}(\Phi) \Phi \bar{\boldsymbol{\mu}}_{k,n}, \quad (10)$$

$$\bar{\boldsymbol{\mu}}_{k,n} = \sum_{n'=1}^{N_k} \alpha_{k,n'} \boldsymbol{\mu}_{k,n'} - \boldsymbol{\mu}_{k,n}, \quad (11)$$

$$\Sigma_{k,n}(\Phi) = \Phi \mathbf{R}_{k,n} \Phi^H + \sigma_k^2 \mathbf{I}_L. \quad (12)$$

Furthermore, const is a term independent of Φ .

Proof: See **Appendix A**.

B. Mutual Information for Sensing

We consider that the ISAC BS listens to backscattering reflections and observes the signal based on two hypothesis. The first being \mathcal{H}_0 , where it assumes the absence of any target, therefore observing interference and background noise. On the other hand, the alternative hypothesis, i.e. \mathcal{H}_1 , where the signal is present and is superimposed on top of interference and background noise. To this end, the ISAC BS listens over L samples and considers the following hypothesis testing problem,

$$\begin{cases} \mathcal{H}_0 : & \mathbf{y}_r = \mathbf{c} + \mathbf{n}_r, \\ \mathcal{H}_1 : & \mathbf{y}_r = \mathbf{d} + \mathbf{c} + \mathbf{n}_r. \end{cases} \quad (13)$$

For convenience, we have directly expressed the hypothesis testing problem using vectorized quantities. In particular, $\mathbf{y}_r = \text{vec}(\mathbf{Y}_r) \in \mathbb{C}^{N_r L \times 1}$, and the signal of interest, i.e. \mathbf{d} , and the clutter vector \mathbf{c} can be expressed as

$$\mathbf{d} = \gamma_0 \text{vec}(\mathbf{a}_{N_r}(\theta_0) \mathbf{a}_{N_t}^T(\theta_0) \Phi^T) \triangleq \gamma_0 \boldsymbol{\mu}_0, \quad (14)$$

$$\mathbf{c} = \sum_{i=1}^Q \gamma_i \text{vec}(\mathbf{a}_{N_r}(\theta_i) \mathbf{a}_{N_t}^T(\theta_i) \Phi^T) \triangleq \sum_{i=1}^Q \gamma_i \boldsymbol{\mu}_i. \quad (15)$$

In practice, multiple sensing target may co-exist. The detection problem herein can be extended to multiple targets by scanning multiple directions in a time division manner. During the training phase for communications, one can optimize the pilots for a set of direction(s), which are to be transmitted to scan the environment. An equivalent, and more convenient, way of expressing the hypothesis test in (13) is

$$\begin{cases} \mathcal{H}_0 : & \mathbf{z} \sim \mathcal{CN}(\mathbf{0}, \mathbf{I}), \\ \mathcal{H}_1 : & \mathbf{z} \sim \mathcal{CN}(\mathbf{0}, (\mathbf{R}_{cc} + \sigma_r^2 \mathbf{I})^{-\frac{1}{2}} \mathbf{R}_{dd} (\mathbf{R}_{cc} + \sigma_r^2 \mathbf{I})^{-\frac{1}{2}} + \mathbf{I}), \end{cases} \quad (16)$$

where \mathbf{R}_{cc} and \mathbf{R}_{dd} are the covariance matrices of \mathbf{c} and \mathbf{d} , respectively. Also, $\mathbf{z} = (\mathbf{R}_{cc} + \sigma_r^2 \mathbf{I})^{-\frac{1}{2}} \mathbf{y}_r$. In general, the larger the MI between the parameters of interest and the observed data, the more information we have about the target of interest [40]. Based on this, we have the following MI-based performance metric for radar sensing,

Proposition 2: For a given pilot matrix Φ and large enough number of receive antennas, i.e. N_r , the MI related to the hypothesis testing problem in (13) can be approximated as $I(\mathbf{Y}_r; \Theta, \boldsymbol{\nu} | \Phi) \simeq \mathcal{M}^{\text{sense}}(\Phi)$, where

$$\mathcal{M}^{\text{sense}}(\Phi) \triangleq \log \left(1 + \frac{\nu_0}{\sigma_r^2} \|\boldsymbol{\mu}_0\|^2 - \frac{\nu_0}{\sigma_r^2} \sum_{i=1}^Q \frac{\nu_i |\boldsymbol{\mu}_0^H \boldsymbol{\mu}_i|^2}{\sigma_r^2 + \nu_i \|\boldsymbol{\mu}_i\|^2} \right), \quad (17)$$

where $\Theta = [\theta_0 \dots \theta_Q]$ and $\boldsymbol{\nu} = [\nu_0 \dots \nu_Q]$.

Proof: See **Appendix B**.

The MI-based performance metric in **Proposition 2** provides various insights. First, the second term appearing in the log is the contribution in the look-direction towards a target of interest located at direction θ_0 . The third term appearing within the log is due to the presence of the Q clutter components.

Therefore, the maximization of the proposed MI-based metric, i.e. $\mathcal{M}^{\text{sense}}(\Phi)$, aims at maximizing the difference between the power found in the look direction and that of the clutter components, in log sense. In the next sub-section, we aim at integrating both MI-based metrics for optimizing communication and sensing performance.

IV. OPTIMIZATION FRAMEWORK FOR ISAC PILOT DESIGN

In this section, we describe an optimization framework enabling us to generate orthogonal pilots that optimize the mutual information for communication and sensing. Since multiple MI-based objectives are to be jointly optimized, an appropriate MOOP [41] can be constructed. To this end, in order to jointly optimize both communication and sensing, we consider the following problem

$$(\mathcal{P}_{\text{MOOP}}) : \begin{cases} \max_{\Phi} & [\mathcal{M}_1^{\text{comm}}(\Phi), \dots, \mathcal{M}_K^{\text{comm}}(\Phi), \mathcal{M}^{\text{sense}}(\Phi)] \\ \text{s.t.} & \Phi \Phi^H = \frac{P}{L} \mathbf{I}, \end{cases} \quad (18)$$

where P is a given power budget. An increase of power budget can indeed translate to an increase in sensing and communication mutual information, as can be inferred from equations (9) and (17). In this paper, we fix the power budget to $\frac{P}{L} = 1$ and aim at optimizing the pilot matrix itself that maximizes both sensing and communication mutual information, without simply increasing power. We note that an assumption of $L < N_t$ is required in order to guarantee an orthonormal solution of the problem in (19). In the system defined by the constraint $\Phi \Phi^H = \mathbf{I}$, there are LN_t unknowns and L^2 equations. Setting $L < N_t$ provides more degrees of freedom than constraints, enabling the optimization of the MI objective in (19) as described in the updated manuscript. Conversely, if $L \geq N_t$, the condition $\Phi \Phi^H = \mathbf{I}$ cannot be satisfied because the rank of $\Phi \Phi^H$ would be limited to N_t .

It is crucial to define an order relation to properly define our MOOP in $(\mathcal{P}_{\text{MOOP}})$. For this, we have

Remark: For any two vectors $\mathbf{a}, \mathbf{b} \in \mathbb{R}^{K+1}$ and $\mathbf{a} \neq \mathbf{b}$, we say that \mathbf{b} *Pareto dominates* \mathbf{a} if and only if $\mathbf{a}_i \leq \mathbf{b}_i$ for all $i = 1 \dots K+1$. This ordering can be denoted as $\mathbf{a} \leq \mathbf{b}$. A "stricter" order can be defined by enforcing a strict inequality component-wise. In both cases, \leq defines a strict partial order on the multidimensional Euclidean space \mathbb{R}^{K+1} . This order relation is commonly referred to as *Pareto order* or *component-wise order* [42].

In equation (18), the MOOP aims at maximizing all sensing and multi-communication MIs simultaneously. This type of optimization problem appears under different names in the literature, such as a vector optimization [43] or multi-criteria optimization [44]. Notice that an orthogonality constraint is enforced on the pilot matrix through $\Phi \Phi^H = \mathbf{I}$ because orthogonal pilot patterns are commonly employed and desired for multi-channel estimation. Generally speaking, orthogonal pilot sequences represent one approach to eliminate the inter-cell interference. In addition, least squares channel estimators become straightforward to implement as no matrix inversion of Φ will be required.

Before we proceed, taking a closer look at problem (18) suggests that the fundamental challenge of directly optimizing

(18) poses a hurdle due to conflicting objectives. In other words, the optimal solution of a given function is $\mathcal{M}_1^{\text{comm}}(\Phi)$ is not necessarily that of $\mathcal{M}^{\text{sense}}(\Phi)$, and improving one can indeed worsen the other. In turn, this means that we may not have a global optimum because there are only subjectively optimal solutions [41]. Technically speaking, the so-called *utopia point*, i.e. the point that maximizes each individual mutual information objective, does not necessarily lie in the attainable objective set [41]. Therefore, the problem is nontrivial and may not have a global optimum. It should be noted that, addressing problem (18) as-is poses technical challenges, it is theoretically possible. A straightforward way would be to sample many feasible pilot matrices satisfying the orthogonality constraint $\Phi\Phi^H = \mathbf{I}$. Besides the heavy complexity involved, this approach does not ensure that any of the sampled pilot matrices lies exactly on the Pareto boundary. Another approach that can be mentioned within this context is the so-called bisection method for Pareto boundary exploration. In short, the bisection method [41] aims to search in given directions and adjust the magnitude of the search vector (through bisection), in order to hit the Pareto frontier. Two challenges can be directly enumerated: (i) The search direction is not-known in advance as the goal is to find the entire set of Pareto points; and (ii) even if we were given the optimal direction, the bisection method involves a membership test, which is itself a complicated problem, as it involves finding the optimal matrix for membership at each iteration. For these reasons, we resort to a linearization method.

Now, since the objective function in (18) is multi-dimensional, we can transform it, utilizing a technique referred to as *scalarization*, with the aid of a goal function [41], hereby denoted as $\psi: \mathbb{R}^{K+1} \rightarrow \mathbb{R}$. More precisely, this goal function describes an ISAC tradeoff between the different MI-based sensing and communication objectives. There are a number of goal function options to be aware of, the simplest being the weighted-sum function, i.e. $\psi(\mathbf{x}) = \sum_k w_k \mathbf{x}_k$. Another choice includes the geometric mean, which is useful when the underlying objectives have different numerical ranges. Since our objectives are all MI-based, hence are of the same nature, then the geometric mean function does not seem to be useful. Other choices are the weighted Chebyshev function and the distance goal function.

Adopting the scalarization technique via weighted-sum, the scalarized version of the MOOP in (18) can be written as

$$(\mathcal{P}_s): \begin{cases} \max_{\Phi} & \mathcal{M}^{\text{ISAC}}(\Phi) \triangleq \rho \mathcal{M}^{\text{comm}}(\Phi) + (1-\rho) \mathcal{M}^{\text{sense}}(\Phi) \\ \text{s.t.} & \Phi\Phi^H = \mathbf{I}. \end{cases} \quad (19)$$

where $\mathcal{M}^{\text{comm}}(\Phi) = \sum_k w_k \mathcal{M}_k^{\text{comm}}(\Phi)$ and $\sum_k w_k = 1$. In the above formulation, the design parameter ρ balances the ISAC tradeoff between sensing, in terms of detection performance seen through $\mathcal{M}^{\text{sense}}(\Phi)$ and the communication channel estimation performance, which is seen through $\mathcal{M}^{\text{comm}}(\Phi)$. In other words, increasing ρ gives a higher priority onto the communication sub-system and decreasing it prioritizes sensing. For communications, the k^{th} user is given a preference associated with value w_k . For equal performance along communication users, one can set $w_1 = \dots = w_K = \frac{1}{K}$.

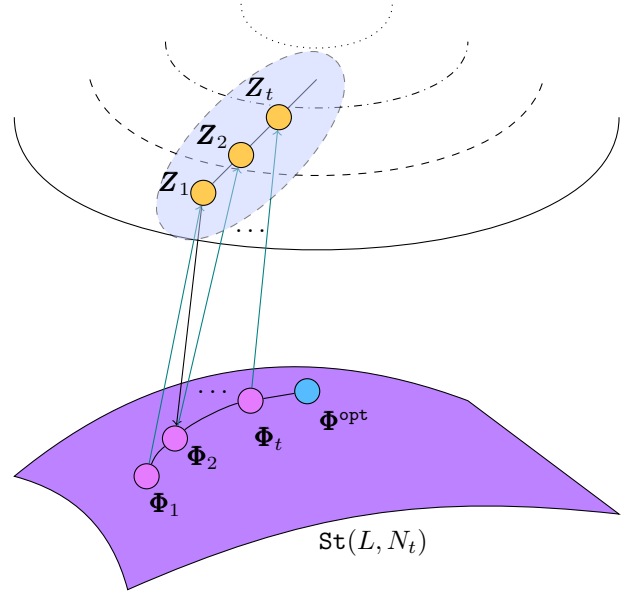


Fig. 2. An illustration depicting the convergence of the projected gradient descent method for ISAC pilot-design. The point Φ^{opt} is the optimal design matrix, which locally maximizes $\mathcal{M}^{\text{ISAC}}(\Phi)$ on the Stiefel manifold.

Observing problem (\mathcal{P}_s) in (19), the cost $\mathcal{M}^{\text{ISAC}}(\Phi)$ in conjunction with the orthogonality constraint leave us with a highly non-convex and non-linear optimization problem. In the next section, we propose an algorithm to directly solve (\mathcal{P}_s) .

V. ISAC PILOT DESIGN BY PROJECTED GRADIENT DESCENT

A. Projected Gradient Descent over the Stiefel Manifold

We design a projected gradient descent method to optimize problem (\mathcal{P}_s) . In other words, the projected gradient descent iterates as follows

$$\mathbf{Z}_{t+1} = \Phi_t + \gamma \nabla_{\Phi} \mathcal{M}^{\text{ISAC}}(\Phi) \Big|_{\Phi=\Phi_t}, \quad (20)$$

$$\Phi_{t+1} = \pi(\mathbf{Z}_{t+1}), \quad (21)$$

where

$$\pi(\mathbf{Y}) = \arg \min_{\mathbf{X} \in \text{St}(L, N_t)} \|\mathbf{X} - \mathbf{Y}\|_F^2. \quad (22)$$

where $\text{St}(N_t, L) = \{\mathbf{X} \in \mathbb{C}^{L \times N_t} : \mathbf{X}\mathbf{X}^H = \mathbf{I}_L\}$ is the Stiefel manifold, which "boils down" to the unit-sphere manifold for $L = 1$. Note that for the case of $N_t > L$, $\pi(\mathbf{Y}) = \mathbf{U}\mathbf{I}_{L, N_t}\mathbf{V}^H$, where $\mathbf{I}_{L, N_t} \in \mathbb{R}^{L \times N_t}$ is a rectangular diagonal matrix with all of its diagonal entries set to 1. Also $\mathbf{Y} = \mathbf{U}\mathbf{\Lambda}\mathbf{V}^H$ represents the singular value decomposition operation. Observe that (20) is a classical gradient descent step and (21) projects the current intermediate point onto the closest point within the feasible set, i.e. the Stiefel manifold, via $\pi(\mathbf{Y})$. In this way, any iteration of the projected gradient algorithm is guaranteed to output an orthogonal pilot, while maximizing the cost $\mathcal{M}^{\text{ISAC}}(\Phi)$.

We now shed light on the gradients, by noting that their expressions can be computed in closed-form. Using the expression defined of $\mathcal{M}^{\text{ISAC}}(\Phi)$ defined in (19), and with the help of (9) and (17), we can write

$$\nabla_{\Phi} \mathcal{M}^{\text{ISAC}}(\Phi) = \rho \sum_k w_k \nabla_{\Phi} \mathcal{M}_k^{\text{comm}}(\Phi) + (1-\rho) \nabla_{\Phi} \mathcal{M}^{\text{sense}}(\Phi), \quad (23)$$

where the expression of $\nabla_{\Phi} \mathcal{M}_k^{\text{comm}}(\Phi)$ is given in **Appendix C** and the expression of $\nabla_{\Phi} \mathcal{M}^{\text{sense}}(\Phi)$ is given in **Appendix D**. At this point, the projected gradient descent method is fully defined and can be executed with the defined gradients. We now analyze the convergence properties of the iterative algorithm.

B. Convergence Properties

Unlike classical analysis, where the cost and the projection set are assumed to be convex, this analysis studies the convergence properties of the projected gradient descent of the non-convex pilot design problem. Before we proceed, we make some assumptions regarding the structure of the function $\mathcal{M}^{\text{ISAC}}(\Phi)$. The following definitions provide lower/upper bounds on specific classes of differentiable, and possibly non-convex, functions.

Definition 1 ([45]): A function $f : \mathbb{R}^n \rightarrow \mathbb{R}$ is said to be $(\alpha, \beta, \epsilon)$ -restricted strongly smooth (RSS) if it is continuously differentiable over a possibly non-convex region $\mathcal{S} \subseteq \mathbb{R}^n$ and for every $\mathbf{x}_1, \mathbf{x}_2 \in \mathcal{S}$, we have that

$$f(\mathbf{x}_2) - f(\mathbf{x}_1) - \nabla f^T(\mathbf{x}_1)(\mathbf{x}_2 - \mathbf{x}_1) \leq \frac{\beta}{2} \|\mathbf{x}_1 - \mathbf{x}_2\|^2 + \frac{\alpha}{2} \epsilon^2. \quad (24)$$

Definition 2 ([45]): A function $f : \mathbb{R}^n \rightarrow \mathbb{R}$ is said to be (α, ϵ) -restricted strongly convex (RSC) if it is continuously differentiable over a possibly non-convex region $\mathcal{S} \subseteq \mathbb{R}^n$ and for every $\mathbf{x}_1, \mathbf{x}_2 \in \mathcal{S}$, we have that

$$f(\mathbf{x}_2) - f(\mathbf{x}_1) - \nabla f^T(\mathbf{x}_1)(\mathbf{x}_2 - \mathbf{x}_1) \geq \frac{\alpha}{2} \|\mathbf{x}_1 - \mathbf{x}_2\|^2 - \frac{\alpha}{2} \epsilon^2. \quad (25)$$

Given the RSC and RSS of a continuously differentiable function, the term ϵ captures the non-convexity of f along $\mathcal{S} \subseteq \mathbb{R}^n$. Indeed, with $\epsilon = 0$, one can see that the function is strongly convex and smooth. Hence, ϵ, α, β can be seen as parameters that trade-off smoothness and convexity. Note that (α, ϵ) -RSC assumptions were also used to establish theoretical results to quantify local optima of regularized estimators, where loss/penalty function are allowed to be non-convex over its associated domain [46].

Provided these definitions, we have the following convergence result on the pilot design projected gradient descent method.

Theorem 1: For any random initialization of the pilot matrix Φ_0 and given α, β, ϵ such that function $-\mathcal{M}^{\text{ISAC}}(\Phi)$ is (α, ϵ) -RSC and $(\alpha, \beta, \epsilon)$ -RSS, the projected gradient descent ISAC-based pilot design algorithm described in (20), (21), (22) converges to Φ_{∞} , such that

$$\mathcal{M}^{\text{ISAC}}(\Phi^{\text{opt}}) - \mathcal{M}^{\text{ISAC}}(\Phi_{\infty}) \leq \frac{\alpha + \frac{\beta}{2} \epsilon^2}{1 - \frac{\beta}{\alpha}} \epsilon^2, \quad (26)$$

where Φ^{opt} is the local maximum of $\mathcal{M}^{\text{ISAC}}(\Phi)$.

Proof: See **Appendix E**.

Therefore, **Theorem 1** reveals that the projected gradient descent method converges to the true maximizer Φ^{opt} , up to a certain precision level controlled by ϵ . An illustration showing the points related to the projected gradient descent method is given in Fig. 2. The pilots generated by the method are projected back onto the Steifel manifold $\text{St}(L, N_t)$ to give Φ_t whenever a new descent update is available, i.e. \mathbf{Z}_{t-1} .

To illustrate the benefits of the proposed algorithm, we

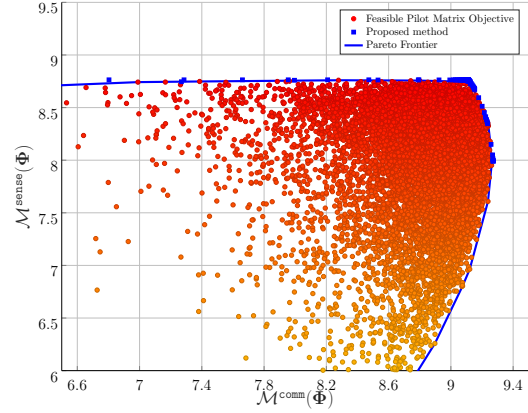


Fig. 3. The feasible pilot matrices region with the corresponding Pareto Frontier and the proposed method that samples on the frontier for different values of ρ . The single-user case.

take a simple single-user example depicted in Fig. 3. This example is intended to show that the proposed projected gradient descent method can efficiently sample the Pareto frontier over different values of sensing and communication balancing parameter ρ . To generate the feasible pilot matrix region, we exhaustively sample over 10000 orthogonal pilot matrices and compute the sensing and communication mutual informations. We then compute the Pareto frontier, followed by launching the proposed method for random initializations for different values of ρ . This simulation tells us that we can almost certainly achieve the Pareto frontier through simple recursion operations dictated in equations (20), (21) and (22), without having to resort to more complicated multi-objective methods.

VI. ON THE ADOPTED MI METRICS: CONNECTIONS & MOTIVATION

A. MI in the context of communication channel estimation

Many natural questions arise at this point. A very fundamental question to ask is the following: "Why would we adopt an MI-based metric for channel estimation?" Another follow-up question can be the following: "How does the adopted MI-based metric relate to the achievable rate?" At first sight, the adopted metric may seem somewhat absurd, however, we show that the adopted MI metric, namely $\mathcal{M}^{\text{comm}}(\Phi)$, directly impacts the achievable rate.

In [47], the authors study the impact of channel estimation errors, taking into account the training time, power allocation strategies between data transmission and training sequence, and the impact these factors have on the capacity of a channel given an estimate of the channel as prior information. In this regard, two stages can be naturally distinguished: (i) the training stage utilizing L time instances where a pilot sequence Φ is passed through the channel \mathbf{H} , where the task here is to estimate the channel, and provide this channel estimation $\hat{\mathbf{H}}$ by observing $\mathbf{Y}_t = \Phi \mathbf{H} + \mathbf{N}_t$, where \mathbf{Y}_t and \mathbf{N}_t are concatenated versions of \mathbf{y}_k and \mathbf{n}_k given in equation (2). The channel estimate is then passed to the subsequent stage where, (ii) the data transmission stage utilizing B data blocks, which uses $\hat{\mathbf{H}}$ as prior information to decode the transmitted

data. Given this, the lower bound (which is tight under certain conditions [47]) on the channel capacity is [47]

$$C_{\text{worst}} = \mathbb{E} \left[\frac{B}{B+L} \log \det \left(\mathbf{I} + \frac{\sigma_{\tilde{\mathbf{H}}}^2}{1 + \sigma_{\tilde{\mathbf{H}}}^2} \frac{\tilde{\mathbf{H}}^* \tilde{\mathbf{H}}^T}{N_t} \right) \right], \quad (27)$$

where $\tilde{\mathbf{H}}$ is the normalized channel estimate, $\sigma_{\tilde{\mathbf{H}}}^2 = \frac{1}{N_t K} \text{tr} \mathbf{R}_{\tilde{\mathbf{H}}}$ is the variance on the channel estimation error, where the error covariance matrix is $\mathbf{R}_{\tilde{\mathbf{H}}} = \mathbb{E} \left[\text{vec}(\tilde{\mathbf{H}})^* \text{vec}(\tilde{\mathbf{H}})^T \right]$ and $\sigma_{\tilde{\mathbf{H}}}^2$ is the variance on the channel estimate. Adopting an MMSE channel estimator, then under the orthogonality principle for MMSE estimates, we can use $\sigma_{\tilde{\mathbf{H}}}^2 = 1 - \sigma_{\hat{\mathbf{H}}}^2$, which in this case, allows us to re-write the effective SNR as $\frac{\sigma_{\tilde{\mathbf{H}}}^2}{1 + \sigma_{\tilde{\mathbf{H}}}^2} = \frac{2}{1 + \sigma_{\hat{\mathbf{H}}}^2} - 1$. Hence, maximizing the worst case channel capacity can be achieved by minimizing $\sigma_{\tilde{\mathbf{H}}}^2$, i.e. minimizing the trace of error covariance matrix of the channel estimate, i.e. $\text{tr} \mathbf{R}_{\tilde{\mathbf{H}}}$. Interestingly, for our adopted communication MI, we have the following

Theorem 2: For a given channel estimation procedure giving $\hat{\mathbf{h}}_k$ by observing \mathbf{y}_k , the quantity $\mathcal{M}_k^{\text{comm}}(\Phi)$ can be lower-bounded as follows

$$\mathcal{M}_k^{\text{comm}}(\Phi) \geq h(\mathbf{h}_k | \Phi) - N_t \log(\pi e) - N_t \log \frac{\text{tr}(\mathbf{R}_{\tilde{\mathbf{h}}_k})}{N_t}, \quad (28)$$

where $\tilde{\mathbf{h}}_k = \mathbf{h}_k - \hat{\mathbf{h}}_k$ and $\mathbf{R}_{\tilde{\mathbf{h}}_k} = \mathbb{E} \left[\tilde{\mathbf{h}}_k \tilde{\mathbf{h}}_k^H \right]$.

Proof: See Appendix F.

It is interesting to see that this lower bound can also be achieved by the estimation-theoretic counterpart of Fano's inequality. Indeed, applying [39] (c.f. Corollary of Theorem 8.6.6), one can obtain $\frac{1}{N_t} \mathbb{E} \left[\|\mathbf{h}_k - \hat{\mathbf{h}}_k\|^2 \right] \geq \frac{1}{\pi e} e^{\frac{1}{N_t} (h(\mathbf{h}_k | \Phi) - \mathcal{M}_k^{\text{comm}}(\Phi))}$. After re-arrangement of terms, we arrive at (28). In fact, the variance on the individual channel estimation errors, i.e. $\sigma_{\tilde{\mathbf{h}}_k}^2 = \frac{1}{N_t} \text{tr} \mathbf{R}_{\tilde{\mathbf{h}}_k}$ is easily verified to relate $\sigma_{\tilde{\mathbf{H}}}^2$ as $\sigma_{\tilde{\mathbf{H}}}^2 = \sum_{k=1}^K \sigma_{\tilde{\mathbf{h}}_k}^2 / K$. From here, a decrease on the variance of channel estimation of the k^{th} user, i.e. $\sigma_{\tilde{\mathbf{h}}_k}^2$, can contribute to an increase of the lower bound of $\mathcal{M}_k^{\text{comm}}(\Phi)$ according to (28). The same decrease $\sigma_{\tilde{\mathbf{h}}_k}^2$ also decreases $\sigma_{\tilde{\mathbf{H}}}^2$, which translates to a direct increase in C_{worst} . This means that, through the intermediate variable $\sigma_{\tilde{\mathbf{h}}_k}^2$, any decrease of $\sigma_{\tilde{\mathbf{H}}}^2$ can simultaneously increase $\mathcal{M}_k^{\text{comm}}(\Phi)$, as well as C_{worst} . To illustrate this influence, we have plotted in Fig. 4 how the behaviour of $\mathcal{M}^{\text{comm}}(\Phi)$ varies with the worst case channel capacity C_{worst} given in (27). It is evident that an increase of worst case channel capacity leads to the direct increase of $\mathcal{M}^{\text{comm}}(\Phi)$, in the long-term. It is worth noting that we have generated random pilot matrices and used them to perform MMSE channel estimation in order to empirically compute (27). We have used these same pilot matrices to compute the MI metric. The increasing trend is also witnessed on varying communication noise levels.

B. MI in the context of sensing

A question that one may ask is "How does the sensing MI adopted in this paper relate to any detection performance metrics?" In this Section, we show that $\mathcal{M}^{\text{sense}}(\Phi)$ is asymptotically related to the probability of detection of the most powerful detection test, according to Neyman-Pearson criterion, under a fixed probability of false alarm. In addition,

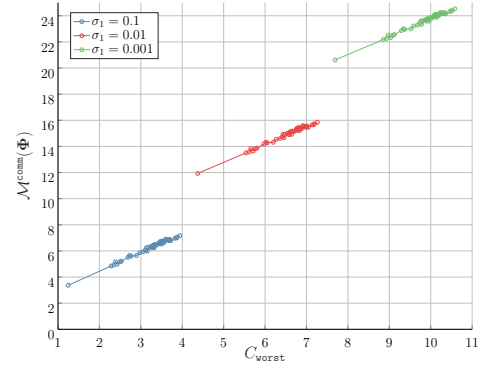


Fig. 4. The proposed MI-based communication metric as a function of worst case channel capacity. Case of single-user and different noise levels.

we also answer a question in the context of parameter estimation, that is "Is there any connection between the considered sensing MI metric and existing estimation performance metrics, such as mean squared error (MSE) or CRB?"

a) Detection tasks

For sensing, this paper focuses on detection rather than estimation. For this, we have the following theorem

Theorem 3: For the most powerful hypothesis test, the function $\mathcal{M}^{\text{sense}}(\Phi)$ relates to the probability of detection as

$$\lim_{L \rightarrow \infty} \left(-\frac{1}{L} \log(1 - P_D) \right) = \mathcal{M}^{\text{sense}}(\Phi) - g(\nu, \Phi), \quad (29)$$

where $g(\nu, \Phi) = \frac{\nu_0 \mu_0^H (\sum_{i=1}^Q \nu_i \mu_i \mu_i^H + \sigma_r^2 \mathbf{I})^{-1} \mu_0}{1 + \nu_0 \mu_0^H (\sum_{i=1}^Q \nu_i \mu_i \mu_i^H + \sigma_r^2 \mathbf{I})^{-1} \mu_0} \geq 0$ and ν is a vector of $\nu_0 \dots \nu_Q$.

Proof: See Appendix G.

The above theorem tells us that $\mathcal{M}^{\text{sense}}(\Phi)$ plays a crucial role, asymptotically with the number of samples and in the large radar signal-to-clutter-plus-noise ratio (SCNR) regime. To be more specific, in the large radar SCNR regime, i.e. when ν_0 grows large with respect to $\nu_1 \dots \nu_Q$ and σ_r^2 , notice that $g(\nu, \Phi)$ converges to 1, i.e. it becomes independent of Φ . In other words, a linear increase in P_D contributes to a logarithmic increase in $\mathcal{M}^{\text{sense}}(\Phi)$ within the prescribed asymptotic regime. This is to say that optimizing $\mathcal{M}^{\text{sense}}(\Phi)$ can influence the detection performance. Within this context, we also note that a result in [48] highlights that higher MI between a parameter and its measurement leads to improved expected performance in the optimal Bayes risk decision procedure.

b) Estimation tasks

Estimation as a sensing task can be also discussed in this Section. Let's say now that the ISAC BS aims at estimating $\xi = [\Theta, \nu]^T$, rather than detecting the presence of a target. Following a similar procedure as the proof of **Theorem 2**, one can lower bound $\mathcal{M}^{\text{sense}}(\Phi)$ as

$$\mathcal{M}^{\text{sense}}(\Phi) \geq h(\xi | \Phi) - \log \left(\det \left(\pi e \mathbf{R}_{\tilde{\xi}} \right) \right) \quad (30)$$

where $\tilde{\xi} = \hat{\xi} - \xi$ and $\mathbf{R}_{\tilde{\xi}} = \mathbb{E} \left[\tilde{\xi} \tilde{\xi}^H \right]$, which tells us that decreasing the error, in the sense of MSE, translates to an increase in the lower bound of the sensing MI. We are also able to relate the sensing MI with the CRB. The CRB inequality tells us that, under the condition that $\hat{\xi}$ is an unbiased estimator

of ξ , we have that

$$\mathbf{R}_{\xi} \succeq \mathcal{F}^{-1} = \left(E \left\{ [\nabla \ln \ell(\mathbf{Y}_r; \xi)] [\nabla \ln \ell(\mathbf{Y}_r; \xi)]^H \right\} \right)^{-1}, \quad (31)$$

where \mathcal{F} is the Fisher information matrix (FIM) and, subsequently, \mathcal{F}^{-1} is the CRB matrix. Also, $\ell(\cdot)$ is the likelihood function. Since \mathcal{F}^{-1} is an error covariance matrix itself, it can replace \mathbf{R}_{ξ} in (30) and so

$$\mathcal{M}^{\text{sense}}(\Phi) \geq h(\xi | \Phi) - N \log \pi e + \log(|\mathcal{F}|). \quad (32)$$

It is worth noting that many previous works have adopted the maximization of the FIM in the determinant sense, such as [31], [49]. Typically, a higher sensing MI allows us to extract more information about the target from the collected measurements, *as though the target were directly communicating its sensing parameters with the ISAC BS.*

C. MI as a unifying ISAC metric

It is tempting to consider a common metric for both sensing and communication, rather than the common way of considering metrics of different nature (e.g. SINR for communications, and CRB or detection probability for sensing). Under the proposed framework, one can treat the overall weighted objective between sensing and communications, given in (19), as a metric under a common unit of measurement, as both the MI-based metric for sensing and that for communications are both measured in bits. The proposed framework of MOOP with a Pareto order relation defined on the \mathbb{R}^{K+1} Euclidean space offers a formal way of combining the MI-based metrics for sensing and communications. Thanks to such a unification, we can extract the overall bits of information for sensing, in terms of detection, and communications, in terms of channel estimation, where the latter has been shown in Section VI-A to impact channel capacity. Also, the proposed projected gradient method described in (20), (21), (22) is computationally efficient, thanks to the combined MI metrics.

VII. SIMULATION RESULTS

In this section, we carry out simulations to demonstrate the MI-based ISAC tradeoffs, as well as the performance advantages of the proposed pilot design method. The array configuration at the ISAC BS follow a ULA fashion for both transmit and receive arrays as shown given in (6) and (7). The central frequency is set to $f_c = 5$ GHz. We take $N_k = 180$ over all K communication users. Following [50], the PDF of each channel component follows a GMM given in (3), where each activation probability is modeled through a Laplacian distribution, i.e. $\alpha_{k,n} = \frac{1}{\sqrt{2}\bar{\sigma}_k} \exp(-\frac{\sqrt{2}|\theta_n - \bar{\theta}_k|}{\bar{\sigma}_k})$, where $\bar{\sigma}_k$ is the azimuth spread characterizing the channel between the ISAC BS and the k^{th} communication user. Also, $\bar{\theta}_k$ represents the mean AoA of the spread of the channel towards the k^{th} user. Each Gaussian component of the GMM is assumed to have a covariance matrix $\mathbf{R}_{k,n} = \int_{\mathcal{R}_n} \mathbf{a}_{N_t}(\theta) \mathbf{a}_{N_t}^H(\theta) d\theta$, where \mathcal{R}_n is the region of over which the n^{th} GMM component is assumed to be observed. These regions are assumed to be disjoint and $\bigcup_n \mathcal{R}_n$ covers $[-90^\circ, +90^\circ]$. Therefore, to generate a random realization of channel \mathbf{h}_k , we first generate $N_k = 180$ Gaussian random realizations, where the n^{th} component has mean $\boldsymbol{\mu}_{k,n}$ and co-variance matrix $\mathbf{R}_{k,n}$, then \mathbf{h}_k is picked based on the activation probabilities $\alpha_{k,n}$. For the single-user case, i.e. $K = 1$, we set the mean AoA

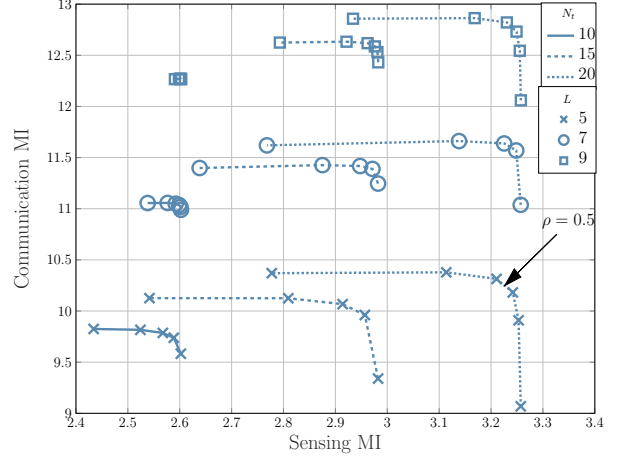


Fig. 5. Achievable sensing and communication MI values for the single-user case by projected gradient descent optimization for different values of N_t and L . The number of receive antennas is set to $N_r = 5$. The target is located at $\theta_0 = 60^\circ$. The radar noise is $\sigma_r = 2$ and the communication noise is $\sigma_1 = 0.1$. No clutter is considered here.

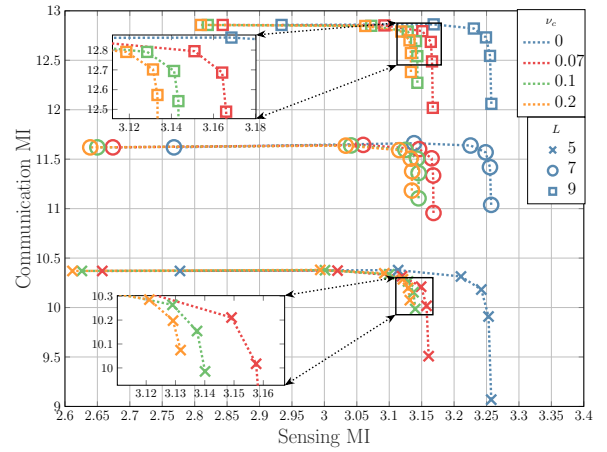


Fig. 6. Clutter impact on the MI ISAC performance for the single-user case and different clutter power ν_c and values of L . We set $\theta_1 = 0^\circ$, $N_r = 5$, $\theta_0 = 60^\circ$, $\sigma_r = 2$ and $\sigma_1 = 0.1$.

component to $\bar{\theta}_1 = 70^\circ$. For the multi-user case, where we have set $K = 4$, we assume that $\bar{\theta}_2 = 23^\circ$, $\bar{\theta}_3 = -23^\circ$, and $\bar{\theta}_4 = -70^\circ$. All communication users are treated equally, therefore $w_k = \frac{1}{K}$. Unless otherwise stated, the projected gradient descent algorithm runs with a step size of $\gamma = 0.1$. As the values of α, ϵ, β are difficult to obtain and reveal convergence towards a stable point, which is a priori unknown, we have set the maximum number of iterations to 200.

a) Impact of N_t and L on the MI ISAC trade-off

In Fig. 5, we study the impact of number of transmit antennas, N_t and number of pilot symbols (pilot length) L on the sensing and communication mutual information. For fixed L and with increasing number of transmit antennas, we can see that both sensing and communication mutual information improve. For example, fixing $L = 5$, we see that maximum communication MI improves from 9.82 bits to 10.12 bits when increasing N_t from 10 to 15 antennas, while the maximum sensing MI rises from 2.6 to 2.98 bits. The same observation

is noticed when going from $N_t = 15$ to $N_t = 20$ for $L = 5$. We set $\sigma_r = 2$. We assume that the single-user communication noise is $\sigma_1 = 0.1$. Furthermore, the azimuth spread is set to $\bar{\sigma}_1 = 6^\circ$. Moreover, the target is located at $\theta_0 = 60^\circ$, and the number of receive antennas is set to $N_r = 5$. Another point worth highlighting is the point corresponding to $\rho = 0.5$, where we have equal priority on communication and sensing performance. We also observe that increasing N_t also contributes to a simultaneous increase in both communication and sensing MI. For $\rho = 0.5$, we observe that for $L = 5$, the sensing MI increases from 2.56 bits to 3.21 bits, while the communication MI increases from 9.78 bits to 10.31 bits, when doubling the number of transmit antennas from 10 to 20. Another factor contributing to the joint ISAC MI gain is L . For instance, focusing on the point corresponding to $\rho = 0.5$ and fixing $N_t = 15$, we observe that the sensing MI increases from 2.91 bits to 2.99 bits, whereas the communication MI increases from 10.06 bits to 12.58 bits, when L increases from 5 to 9. An interesting phenomenon worth highlighting is the achievable range of ISAC tradeoffs, as a function of N_t and L . For example, when $L = 9$, we notice that increasing N_t not only improves the ISAC MI, but also allows the designer to achieve a wider set of sensing and communication MI values for different ISAC pilot matrices. Indeed, notice that for $N_t = 10$ and $L = 9$, the trade-off achieves sensing MI values that are within $[2.59, 2.61]$, whereas communication MI values are within $[12.265, 12.27]$. Both range of values can be increased by increasing N_t , thus allowing for more ISAC trade-offs.

b) Impact of clutter on the MI ISAC trade-off

In Fig. 6, we highlight how clutter can influence the ISAC performances from a mutual information perspective. The same simulation parameters as in Fig. 5, with the exception of the clutter setting. In particular, to study the impact of clutter, we set $Q = 1$ and denote $\nu_c = \nu_1$. We vary the values of ν_c to analyze the clutter impact. The clutter is assumed to be located at $\theta_1 = 0^\circ$. We can see that for fixed N_t and L , an increase in ν_c causes the sensing MI to decrease without majorly impacting the communication MI. Despite the presence of clutter, we see that the sensing MI is still relatively high enough, hence detection can still be reliably performed. Fixing L to 5, we see that a clutter component with $\nu_c = 0.07$ deteriorates the maximal sensing MI from 3.25 to 3.16 bits compared to the no-clutter case. On the other hand, the maximal communication MI is at 10.37 bits regardless of the clutter power. When equal priority is set on sensing and communication, increasing L can aid in improving the sensing performance. For example, the sensing MI increases from 3.14 to 3.16 bits when increasing L from 5 to 9. Similar observations can be reported for increasing ν_c .

c) Target location can improve MI ISAC gains

In Fig. 7, we aim at studying the target position and its impact on the sensing and communication MI tradeoffs. The single-user case is assumed with $L = 10$ and number of receive antennas $N_r = 70$ at the ISAC BS. We set $\sigma_1 = 0.1$ and $\sigma_r = 0.002$. The frontiers are generated by sweeping over multiple values of ρ . The different frontiers are generated by changing the target's location. The user

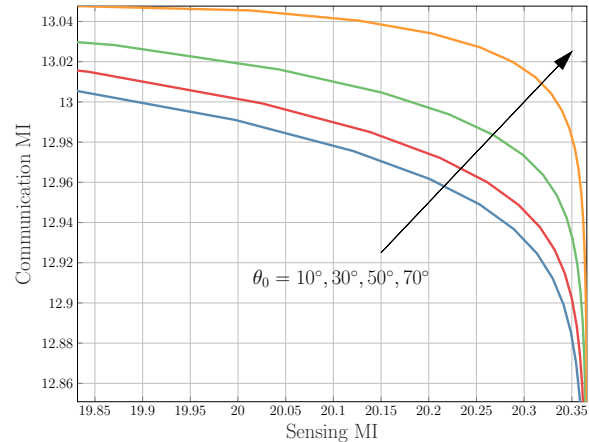


Fig. 7. The impact of the target AoA on the ISAC trade-off for the single-user case. We plot 4 MI-frontiers where the blue frontier corresponds to $\theta_0 = 10^\circ$ and the orange corresponds to $\theta_0 = 70^\circ$. We set $N_r = 70$, $L = 10$. We have $\sigma_1 = 0.1$ and $\sigma_r = 0.002$. The user is located around $\bar{\theta}_1 = 70^\circ$.

is located around $\bar{\theta}_1 = 70^\circ$. In particular, we vary the target AoA by bringing it closer towards the mean of the communication user AoA. Indeed, the closer the target is brought towards the user, the boundary approach a utopia point, i.e. achieving maximal sensing and communication MI performance with the same orthogonal pilot symbols. This can be explained by some sensing and communication *information overlap* between the communication channel \mathbf{h}_k and part of the sensing channel characterized by the AoAs Θ and the path gains ν . Note that a similar phenomenon is reported in [11], where a sensing and communication *subspace overlap* can also improve communication-rate and sensing performance. The study, herein, serves as a complementary one as pilots can provide better channel estimates when the target approaches the communication user. The best performance is observed when the target and communication user are at the same location, which is an interesting use case when the objective is to sense a communication user, hence the integration gain is fully exploited.

d) ROC performance of pilot matrices

In this part, we generate ROC curves through Monte Carlo simulations. In particular, every point of probability of false alarm and detection probability pair (P_{fa}, P_d) is obtained using 10^6 Monte Carlo trials. In Fig. 8, we take a step further and utilize the generated pilot symbols to evaluate the performance of the ROC via the optimal detector reported in [51]. In particular, the figure shows the ROC curves for different values of ρ and compares the ROC performance to a non-optimized and orthogonal pilot matrix. To this end, we set the pilot length is $L = 9$. Moreover, the number of transmit and receive antennas at the ISAC BS are set to $N_t = 20$ and $N_r = 5$ antennas, respectively. It is clear that optimizing the pilot matrix via the proposed projected gradient method can improve the detection capabilities performed at the ISAC BS through the same pilot matrix used for communications. For this simulation, the target is located at $\theta_0 = 60^\circ$ and the communication noise level is $\sigma_1 = 0.1$. As an example, if the designer sets a probability of false alarm at $P_{fa} = 10^{-4}$ and generates an orthogonal pilot

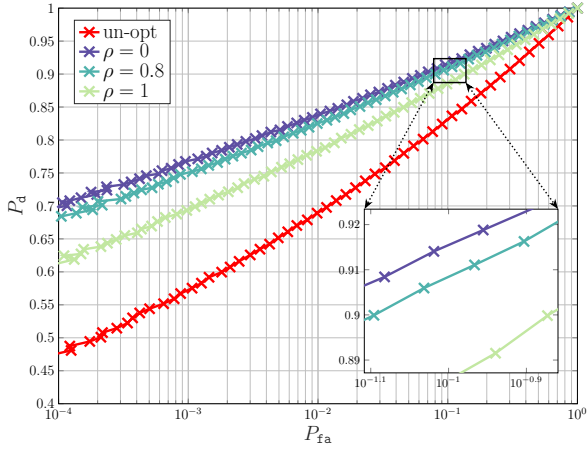


Fig. 8. Receiver operating characteristic curves for different values of ρ and for an non-optimized and orthogonal pilot, i.e. random but orthogonal, for $\sigma_r = 2$. The single-user case is considered with $N_t = 20$ and $N_r = 5$ antennas. The pilot length is $L = 9$. The target is located at $\theta_0 = 60^\circ$ and $\sigma_1 = 0.1$.

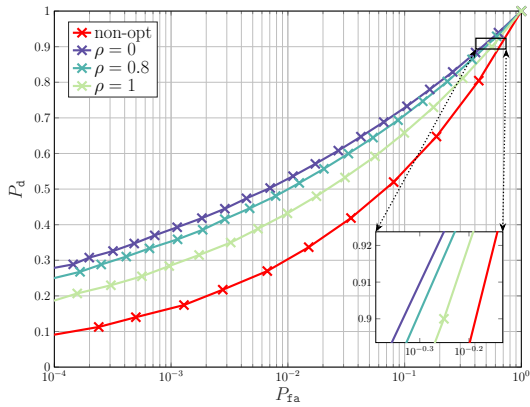


Fig. 9. Receiver operating characteristic curves for different values of ρ and for an non-optimized and orthogonal pilot for $\sigma_r = 4$. All other simulation parameters are the same as those in Fig. 8.

matrix by the proposed method for $\rho = 1$ (communication-optimal), the achieved probability of detection is $P_d = 0.61$, which is greater than that of an non-optimized orthogonal pilot, which achieves $P_d = 0.475$. Note that, even though the priority is set to the communication task (i.e. channel estimation), the optimized pilot generated by the proposed method can still outperform an non-optimized one. If the designer seeks a better detection performance, then this can be achieved by lowering ρ , hence giving more priority towards sensing. Indeed, with $\rho = 0.8$ and for the same $P_{fa} = 10^{-4}$, the P_d increases from 0.61 to 0.68 and can reach $P_d = 0.7$ for $\rho = 1$. Similar observations are noticed for any false-alarm probability.

In Fig. 9, we increase the radar noise to $\sigma_r = 4$. All other simulation parameters are exactly the same as those in Fig. 8. Indeed, due to a more noisy radar sub-system, the detector has to increase the probability of false alarm to achieve the same detection probability performance as those specified in Fig. 8 (i.e. $\sigma_r = 2$) for $P_d = 0.475$. Given that, increasing the

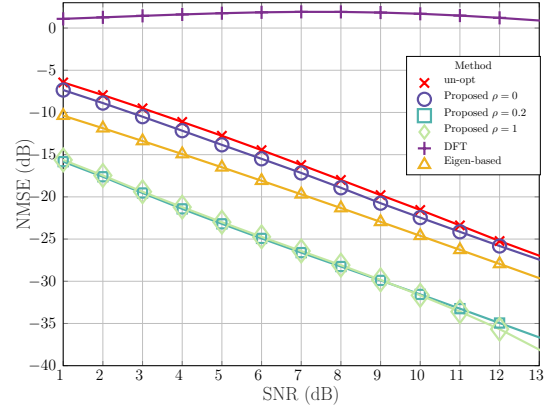


Fig. 10. NMSE performance of the generated pilots compared to an unoptimized orthogonal pilot matrix for different number of communication users and different values of ρ .

P_{fa} level to $P_{fa} = 5 \times 10^{-2}$, the non-optimized pilot achieves $P_d = 0.475$, whereas the proposed method for $\rho = 1$ generates an orthogonal pilot with $P_d = 0.59$ capabilities. If a larger detection probability is desired, one would have to decrease ρ thus achieving $P_d = 0.64$ for $\rho = 0.8$ and $P_d = 0.67$ for $\rho = 1$. We have identical observations for different false-alarm levels.

e) NMSE performance

In Fig. 10, we assess the NMSE performance of the generated orthogonal pilot matrices in order to study its channel estimation capability with different number of communication users, i.e. K , and different values of ρ . To this end, the NMSE is evaluated as

$$\text{NMSE} = \frac{1}{KR} \sum_{k=1}^K \sum_{r=1}^R \frac{\|\mathbf{h}_{k,r} - \hat{\mathbf{h}}_{k,r}^{\text{MMSE}}\|^2}{\|\mathbf{h}_{k,r}\|^2}, \quad (33)$$

where $\mathbf{h}_{k,r}$ is the communication channel between the ISAC BS and the k^{th} user generated at the r^{th} Monte-Carlo trial, and $\hat{\mathbf{h}}_{k,r}^{\text{MMSE}}$ is its MMSE estimate, which is a widely adopted figure of merit in signal processing [52]. As a reminder, the MMSE estimate minimizes $\mathbb{E}[\|\mathbf{h}_{k,r} - \hat{\mathbf{h}}_{k,r}\|^2]$ with respect to $\hat{\mathbf{h}}_{k,r}$ and is obtained via the following marginalization as follows [53]

$$\begin{aligned} \hat{\mathbf{h}}_{k,r}^{\text{MMSE}} &\triangleq \mathbb{E}[\mathbf{h}_{k,r} | \mathbf{y}_{k,r}] \\ &= \sum_{n=1}^{N_k} p_{k,n,r} (\boldsymbol{\mu}_{k,n} + \mathbf{R}_{k,n} \boldsymbol{\Phi}^H \boldsymbol{\Sigma}_{k,n}^{-1}(\boldsymbol{\Phi}) (\mathbf{y}_{k,r} - \boldsymbol{\Phi} \boldsymbol{\mu}_{k,n})), \end{aligned} \quad (34)$$

where $\mathbf{y}_{k,r} \in \mathbb{C}^{L \times 1}$ is the received signal at the k^{th} user on the r^{th} trial following (2). Moreover, $\boldsymbol{\Sigma}_{k,n}(\boldsymbol{\Phi})$ is given in equation (12). The probabilities at the r^{th} trial $p_{k,n,r}$ (also referred to as *responsibilities*) are computed via

$$p_{k,n,r} = \frac{\alpha_{k,n} f_{\text{CN}}(\mathbf{y}_{k,r} | \boldsymbol{\Phi} \boldsymbol{\mu}_{k,n}, \boldsymbol{\Sigma}_{k,n}(\boldsymbol{\Phi}))}{\sum_{n'=1}^{N_k} \alpha_{k,n'} f_{\text{CN}}(\mathbf{y}_{k,r} | \boldsymbol{\Phi} \boldsymbol{\mu}_{k,n'}, \boldsymbol{\Sigma}_{k,n'}(\boldsymbol{\Phi}))}. \quad (35)$$

Fig. 10 shows the resulting NMSE performance for the single-user case, when compared to multiple benchmarks, i.e. (i) discrete Fourier transform (DFT) sequence used for pilot design [54], i.e. columns drawn out from the DFT matrix and (ii) an eigen-based design whereby the strongest L eigenvectors are computed from the overall covariance matrix of the channel to construct the orthogonal pilots [55], and (iii) a non-optimized but orthogonal pilot matrix. We have fixed $N_t = 40$ and

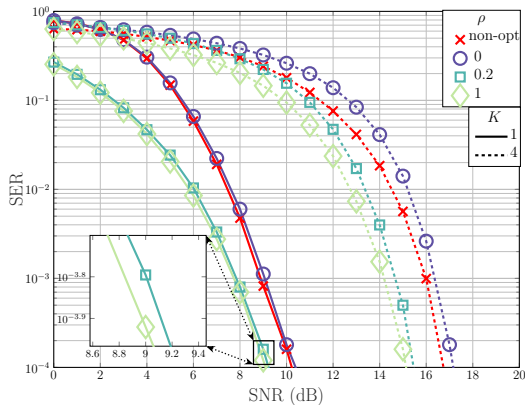


Fig. 11. SER performance of the generated pilots compared to an unoptimized orthogonal pilot matrix for different values of ρ and different number of communication users. A 64-QAM with Gray encoding is used for data modulation.

$N_r = 70$ antennas. The azimuth spread is set to $\bar{\sigma}_k = 4^\circ$ per user. We have fixed the target at $\theta_0 = -20^\circ$, and set $L = 10$. From Fig. 10, it is observed that the NMSE performance of the non-optimized pilot matrix closely matches that of the pilot matrix designed using the proposed method with $\rho = 0$ (sensing-optimal configuration). We also see in that case that the eigen-based pilot design outperforms the non-optimized pilot design by 2 dB and the proposed pilot for $\rho = 0$ by about 1.7 dB gain, in terms of SNR. Increasing ρ to 0.2 achieves a performance level comparable to the communication-optimal pilot matrix ($\rho = 1$), which provides an approximate gain of 6 dB over the non-optimized pilot matrix and a 4 dB gain over the eigen-based pilot design. We also see that the DFT sequence has the worst-performance as also reported in [54], but to further improve DFT sequence performance in terms of channel estimation, it should be combined with range matching pursuit [54].

f) SER performance

In Fig. 11, we evaluate the SER performance of the generated orthogonal pilot matrices and observe the gains in SER as compared to the non-optimized pilot matrix as a function of SNR and for different values of ρ and number of communication users, i.e. K . The same simulation parameters are used as those in Fig. 10. For communications, a 64-QAM was used as constellation for digital modulation with gray encoding. The MMSE channel estimator in (34) and (35) is first utilized to estimate the channel, then a ZF equalizer is used to demodulate the symbol using a hard-decision decoder. For the single-user case, and setting the SER level to 10^{-4} , we see that the SER performance of the non-optimized pilot matrix is 0.15 dB better than that of the pilot matrix generated by the proposed method for $\rho = 0$ (sensing-optimal). We can improve the SER by 1 dB by increasing ρ to 0.2. An additional gain of about 0.1 dB can be achieved by increasing ρ to 1. As for the multi-user case for $K = 4$, better gains can be reported, even though the non-optimized pilot gains 0.5 dB as compared to pilot matrix generated by the proposed method for $\rho = 0$. For example, setting the SER level to 10^{-4} and $\rho = 0.2$, we can gain 1.3 dB of SNR as compared to the non-optimized

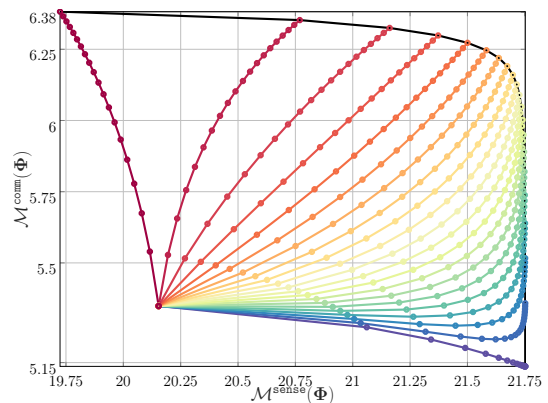


Fig. 12. The convergence behavior of the proposed method in terms of $\mathcal{M}^{\text{comm}}(\Phi)$ and $\mathcal{M}^{\text{sense}}(\Phi)$. Each colored path represents the path taken for a fixed ρ . Each point corresponds to a pilot matrix generated by the method. The initial point at $(20.15, 5.34)$ is the initial point shared for all paths. The black line represents the frontier joining the converged points spanning $\rho = 0 \dots 1$, i.e. an approximation of the Pareto frontier.

pilot and 1.6 dB if we fix $\rho = 1$. Therefore, we can report more SNR gains with increasing number of communication users.

g) Convergence behaviour

In Fig. 12, the convergence behavior of the projected gradient descent method for different values of ρ , in terms of $\mathcal{M}^{\text{sense}}(\Phi)$ and $\mathcal{M}^{\text{comm}}(\Phi)$ is presented. We choose the same initial pilot for different ρ to study the path taken by the proposed method. A single-user case is analyzed, where the simulation parameters are the same as the single-user case in Fig. 10. The communication noise level is set to $\sigma_1 = 0.2$. We set the azimuth spread to $\bar{\sigma}_1 = 6^\circ$. The step-size is $\gamma = 0.1$. The figure was generated for each ρ where we store each generated pilot per iteration, and subsequently compute $\mathcal{M}^{\text{comm}}(\Phi)$ using (9) and $\mathcal{M}^{\text{sense}}(\Phi)$ via (17). Therefore, each path corresponds to a different values of ρ . We have 21 paths simulated by increasing ρ a value of 0.05 each time. It is evident that, for any value of ρ , the proposed method is ensured to converge to a fixed point. In addition, it is noteworthy that all paths eventually converge to a stable frontier. For instance, when $\rho = 0$, the method converges to an orthogonal pilot matrix whose sensing and communication MI values are $(21.75, 5.14)$. When $\rho = 0.5$, we converge to $(21.72, 6.08)$ and $(19.72, 6.38)$ when $\rho = 1$. This shows that the algorithm is able to tradeoff between sensing and communications.

Next, in Fig. 13, we plot the cost convergence versus the iteration number. We run the algorithm for 200 iterations and for different values of step-size, γ . We see that for both values of γ , the method converges to a stable value of $\mathcal{M}^{\text{ISAC}}(\Phi) = 18$. Moreover, when $\gamma = 0.5$, the convergence is reported to be faster as the method can converge with about 50 iterations.

VIII. CONCLUSIONS AND RESEARCH DIRECTIONS

This paper formulated a thorough ISAC framework for designing orthogonal pilots tailored for communication and sensing purposes. With the help of mutual information quantities, we designed orthogonal pilots that are optimized for both communication and target detection. For this, a multi-objective optimization problem has been formulated to model the pilot design problem at hand. Nevertheless, a scalarization

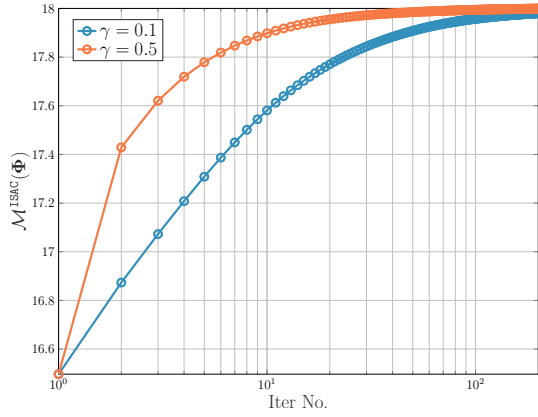


Fig. 13. The impact of the step size on the convergence behavior of the projected gradient descent for ISAC pilot design.

procedure was adopted, followed by an algorithmic description based on projected gradient descent was derived to generate our ISAC orthogonal pilots. Our analysis also reveals that the proposed design is guaranteed to converge to a stable orthogonal pilot. In addition, simulation results unveil the full dual potential of the design pilots, as well as the ISAC tradeoffs the framework has to offer.

Future research will be oriented towards pilot generation with additional practical properties, such as good synchronization properties and low PAPR. A possible direction may also be to utilize artificial intelligence and deep learning techniques for pilot generation, offering various features, which include but are not limited to multi-target detection and channel tracking.

APPENDIX A EXPRESSION OF $\mathcal{M}_k^{\text{comm}}(\Phi)$

This part of the appendix re-writes the mutual information between the received signal at the k^{th} communication user and the channel between the ISAC BS and the k^{th} communication user. To this end, we have the following set of equalities and approximations

$$\begin{aligned}
 I(\mathbf{y}_k; \mathbf{h}_k) &= h(\mathbf{y}_k) - h(\mathbf{y}_k | \mathbf{h}_k) \\
 &\stackrel{\text{(a)}}{=} -\mathbb{E}[\log \phi_y(\mathbf{y}_k)] - \mathbb{E}[\log \phi_y(\mathbf{y}_k | \mathbf{h}_k)] \\
 &\stackrel{\text{(b)}}{\approx} -\mathbb{E}[\log \phi_y(\bar{\mathbf{y}}_k) + \mathbf{d}^H(\bar{\mathbf{y}}_k) [\mathbf{y}_k - \bar{\mathbf{y}}_k]] - \mathbb{E}[\log \phi_y(\mathbf{y}_k | \mathbf{h}_k)] \\
 &\stackrel{\text{(c)}}{=} -\log \phi_y(\bar{\mathbf{y}}_k) - \mathbf{d}^H(\bar{\mathbf{y}}_k) [\mathbb{E}[\mathbf{y}_k] - \bar{\mathbf{y}}_k] - \mathbb{E}[\log \phi_y(\mathbf{y}_k | \mathbf{h}_k)] \\
 &\stackrel{\text{(d)}}{=} -\log \left(\sum_{n=1}^{N_k} \alpha_{k,n} \phi_n(\bar{\mathbf{y}}_k) \right) - \mathbb{E}[\log \phi_y(\mathbf{y}_k | \mathbf{h}_k)] \\
 &\stackrel{\text{(e)}}{=} -\log \left(\sum_{n=1}^{N_k} \frac{\alpha_{k,n} e^{-\bar{\boldsymbol{\mu}}_{k,n}^H \Phi^H \Sigma_{k,n}^{-1}(\Phi) \Phi \bar{\boldsymbol{\mu}}_{k,n}}}{\det(\Sigma_{k,n}(\Phi))} \right) + \text{cnst}.
 \end{aligned} \tag{36}$$

In (36), step (a) follows from the definition of differential entropy and conditional differential entropy, respectively. Note that ϕ_y is the PDF describing random variable \mathbf{y}_k , i.e. $\mathbf{y}_k \sim \phi_y$. Step (b) linearizes the log function through a 1st order Taylor expansion around the mean of \mathbf{y}_k , i.e.

$$\bar{\mathbf{y}}_k = \mathbb{E}[\mathbf{y}_k] = \sum_{n=1}^{N_k} \alpha_{k,n} \Phi \boldsymbol{\mu}_{k,n}, \tag{37}$$

where $\mathbf{d}(\mathbf{y})$ is the gradient of $\log \phi_y(\mathbf{y})$ with respect to \mathbf{y} . Step (c) applies the expectation onto random variable \mathbf{y}_k . Step (d)

uses $\bar{\mathbf{y}}_k \triangleq \mathbb{E}[\mathbf{y}_k]$ and uses the fact that \mathbf{y}_k is also a GMM, whose PDF is given as

$$\phi_y(\mathbf{y}_k) = \sum_{n=1}^{N_k} \alpha_{k,n} \phi_n(\mathbf{y}_k), \tag{38}$$

where it is easy to show that each Gaussian component ϕ_n is $\phi_n(\mathbf{y}_k) = f_{\mathcal{CN}}(\mathbf{y}_k | \Phi \boldsymbol{\mu}_{k,n}, \Sigma_{k,n}(\Phi))$, and the expression of $\Sigma_{k,n}(\Phi)$ is given in (12). Furthermore, we evaluate $\phi_y(\mathbf{y})$ in (38) at $\bar{\mathbf{y}}_k$ given in (37) to obtain $\phi_n(\bar{\mathbf{y}}_k)$ in step (d) in (36). Indeed, after some straightforward linear algebra, we can show

$$\phi_n(\bar{\mathbf{y}}_k) = \frac{1}{\pi^L \det(\Sigma_{k,n}(\Phi))} \times \exp(-\bar{\boldsymbol{\mu}}_{k,n}^H \Phi^H \Sigma_{k,n}^{-1}(\Phi) \Phi \bar{\boldsymbol{\mu}}_{k,n}), \tag{39}$$

where the expression of $\bar{\boldsymbol{\mu}}_{k,n}$ is given in (11). Finally, injecting (39) in the first term of step (d) in (36), we arrive at step (e), where $\text{cnst} = L \log \pi - L \log(\pi \sigma_k^2 e)$. The first term in cnst is due to the π^L appearing in the denominator of (39), whereas the second term is due to the fact that the differential entropy conditioned over the channel can be written as $\mathbb{E}[\log \phi_y(\mathbf{y}_k | \mathbf{h}_k)] = \mathbb{E}[\log \phi_y(\mathbf{y}_k - \Phi \mathbf{h}_k | \mathbf{h}_k)] = \mathbb{E}[\phi_n(\mathbf{n}_k | \mathbf{h}_k)] = -L \log(\pi \sigma_k^2 e)$, since \mathbf{n}_k is a complex Gaussian distribution.

APPENDIX B EXPRESSION OF $\mathcal{M}^{\text{sense}}(\Phi)$

In this appendix, we express the mutual information for sensing in terms of power quantities of the target of interest and clutter, as well as the cross-correlations between target of interest and the clutter. Therefore, we have the following set of equalities

$$\begin{aligned}
 \mathcal{M}^{\text{sense}}(\Phi) &\triangleq I(\mathbf{Y}_r; \Theta, \nu | \Phi) \stackrel{\text{(a)}}{=} h(\mathbf{Y}_r | \Phi) - h(\mathbf{Y}_r | \Phi, \Theta, \nu) \\
 &\stackrel{\text{(b)}}{=} \log \left[(\pi e)^{N_r} \det \left\{ (\mathbf{R}_{cc} + \sigma_r^2 \mathbf{I})^{-\frac{1}{2}} \mathbf{R}_{dd} (\mathbf{R}_{cc} + \sigma_r^2 \mathbf{I})^{-\frac{1}{2}} + \mathbf{I} \right\} \right] \\
 &\quad - \log \left((\pi e)^{N_r} \det \{ \mathbf{I} \} \right) \\
 &\stackrel{\text{(c)}}{=} \log \left[\det \left\{ (\mathbf{R}_{cc} + \sigma_r^2 \mathbf{I})^{-1} \mathbf{R}_{dd} + \mathbf{I} \right\} \right] \\
 &\stackrel{\text{(d)}}{=} \log \left(1 + \nu_0 \boldsymbol{\mu}_0^H \left(\sum_{i=1}^Q \nu_i \boldsymbol{\mu}_i \boldsymbol{\mu}_i^H + \sigma_r^2 \mathbf{I} \right)^{-1} \boldsymbol{\mu}_0 \right) \\
 &\stackrel{\text{(e)}}{\approx} \log \left(1 + \frac{\nu_0}{\sigma_r^2} \|\boldsymbol{\mu}_0\|^2 - \sum_{i=1}^Q \frac{\nu_0 \nu_i \boldsymbol{\mu}_0^H \boldsymbol{\mu}_i}{\sigma_r^2 + \nu_i \|\boldsymbol{\mu}_i\|^2} \right).
 \end{aligned} \tag{40}$$

In step (a), we applied the definition of mutual information. In step (b), we followed the definition of (conditional) differential entropy, and used the equivalence between (13) and (16). In step (c), we used $\det(\mathbf{I} + \mathbf{A}\mathbf{B}) = \det(\mathbf{I} + \mathbf{B}\mathbf{A})$. In step (d), we used $\det(\mathbf{I} + \mathbf{A}\mathbf{x}\mathbf{x}^H) = 1 + \mathbf{x}^H \mathbf{A} \mathbf{x}$, and we expressed the covariance matrices in terms of $\boldsymbol{\mu}_i$, for all $i = 0 \dots Q$, i.e. $\mathbf{R}_{dd} = \nu_0 \boldsymbol{\mu}_0 \boldsymbol{\mu}_0^H$ and $\mathbf{R}_{cc} = \sum_{i=1}^Q \nu_i \boldsymbol{\mu}_i \boldsymbol{\mu}_i^H$. In step (e), we have applied the Woodbury matrix identity, i.e. $(\mathbf{I} + \mathbf{U}\mathbf{U}^H)^{-1} = \mathbf{I} - \mathbf{U}(\mathbf{I} + \mathbf{U}^H \mathbf{U})^{-1} \mathbf{U}^H$, where $\mathbf{U} = \begin{bmatrix} \frac{\sqrt{\nu_1}}{\sigma_r} \boldsymbol{\mu}_1 & \dots & \frac{\sqrt{\nu_Q}}{\sigma_r} \boldsymbol{\mu}_Q \end{bmatrix}$ and approximated $\mathbf{U}^H \mathbf{U}$ to be diagonal, which is valid when N_r grows large.

APPENDIX C EXPRESSION OF $\nabla_{\Phi} \mathcal{M}_k^{\text{comm}}(\Phi)$

In this part of the appendix, we derive the gradient expression of $\mathcal{M}_k^{\text{comm}}(\Phi)$ with respect to Φ . Using matrix-based

gradient identities, we have the following set of equations $\nabla_{\Phi} \mathcal{M}_k^{\text{comm}}(\Phi)$

$$\begin{aligned}
&= -\nabla_{\Phi} \log d_{k,n} = -\omega_k^{-1}(\Phi) \sum_{n=1}^{N_k} \nabla_{\Phi} d_{k,n} \\
&= -\omega_k^{-1}(\Phi) \sum_{n=1}^{N_k} \alpha_{k,n} \nabla_{\Phi} \left[\frac{1}{\det(\Sigma_{k,n}(\Phi))} \right] e^{-\beta_{k,n}(\Phi)} \\
&\quad - \omega_k^{-1}(\Phi) \sum_{n=1}^{N_k} \alpha_{k,n} \frac{1}{\det(\Sigma_{k,n}(\Phi))} \nabla_{\Phi} e^{-\beta_{k,n}(\Phi)} \\
&= \omega_k^{-1}(\Phi) \sum_{n=1}^{N_k} \alpha_{k,n} \frac{\nabla_{\Phi} \det(\Sigma_{k,n}(\Phi))}{\det^2(\Sigma_{k,n}(\Phi))} e^{-\beta_{k,n}(\Phi)} \\
&\quad + \omega_k^{-1}(\Phi) \sum_{n=1}^{N_k} \alpha_{k,n} \frac{\nabla_{\Phi} \beta_{k,n}(\Phi)}{\det(\Sigma_{k,n}(\Phi))} e^{-\beta_{k,n}(\Phi)} \\
&= \omega_k^{-1}(\Phi) \sum_{n=1}^{N_k} d_{k,n} \left\{ \frac{\nabla_{\Phi} \det(\Sigma_{k,n}(\Phi))}{\det(\Sigma_{k,n}(\Phi))} + \nabla_{\Phi} \beta_{k,n}(\Phi) \right\} \\
&= \omega_k^{-1}(\Phi) \sum_{n=1}^{N_k} d_{k,n} \left\{ \Sigma_{k,n}^{-1}(\Phi) \nabla_{\Phi} \Sigma_{k,n}(\Phi) + \nabla_{\Phi} \beta_{k,n}(\Phi) \right\} \\
&= 2\omega_k^{-1}(\Phi) \sum_{n=1}^{N_k} d_{k,n} \Sigma_{k,n}^{-1}(\Phi) \Phi \mathbf{R}_{k,n} \\
&\quad - 2\omega_k^{-1}(\Phi) \sum_{n=1}^{N_k} d_{k,n} \mathbf{R}_{k,n} \Phi^H \Sigma_{k,n}^{-1}(\Phi) \Phi \bar{\boldsymbol{\mu}}_{k,n} \bar{\boldsymbol{\mu}}_{k,n}^H \Phi^H \Sigma_{k,n}^{-1}(\Phi) \\
&\quad + 2\omega_k^{-1}(\Phi) \sum_{n=1}^{N_k} d_{k,n} \bar{\boldsymbol{\mu}}_{k,n} \bar{\boldsymbol{\mu}}_{k,n}^H \Phi^H \Sigma_{k,n}^{-1}(\Phi), \tag{41}
\end{aligned}$$

where $\omega_k(\Phi) = \sum_{n=1}^{N_k} d_{k,n}$ and $d_{k,n} = \frac{\alpha_{k,n} e^{-\beta_{k,n}(\Phi)}}{\det(\Sigma_{k,n}(\Phi))}$ have been introduced for sake of compact notation.

APPENDIX D

EXPRESSION OF $\nabla_{\Phi_l} \mathcal{M}^{\text{sense}}(\Phi)$

In this part of the appendix, we derive the gradient of $\mathcal{M}^{\text{sense}}(\Phi)$ with respect to the l^{th} pilot vector Φ_l . Due to the log structure, it is easily verified that we can write

$$\begin{aligned}
\nabla_{\Phi_l} \mathcal{M}^{\text{sense}}(\Phi) &= \frac{\frac{\nu_0}{\sigma_r^2} \nabla_{\Phi_l} \|\boldsymbol{\mu}_0\|^2 - \frac{\nu_0}{\sigma_r^2} \sum_{i=1}^Q \nabla_{\Phi_l} \frac{\nu_i \boldsymbol{\mu}_0^H \boldsymbol{\mu}_i}{\sigma_r^2 + \nu_i \|\boldsymbol{\mu}_i\|^2}}{1 + \frac{\nu_0}{\sigma_r^2} \|\boldsymbol{\mu}_0\|^2 - \frac{\nu_0}{\sigma_r^2} \sum_{i=1}^Q \frac{\nu_i \boldsymbol{\mu}_0^H \boldsymbol{\mu}_i}{\sigma_r^2 + \nu_i \|\boldsymbol{\mu}_i\|^2}}. \tag{42}
\end{aligned}$$

Using the following expressions

$$\nabla_{\Phi_l} \|\boldsymbol{\mu}_i\|^2 = 2\mathbf{A}^H(\theta_i) \mathbf{A}(\theta_i) \Phi_l, \tag{43}$$

$$\nabla_{\Phi_l} \boldsymbol{\mu}_i^H \boldsymbol{\mu}_j = \mathbf{A}^H(\theta_i) \mathbf{A}(\theta_j) \Phi_l + \mathbf{A}^H(\theta_j) \mathbf{A}(\theta_i) \Phi_l, \tag{44}$$

$$\nabla_{\Phi_l} |\boldsymbol{\mu}_i^H \boldsymbol{\mu}_j|^2 = 2\Re[\boldsymbol{\mu}_i^H \boldsymbol{\mu}_j] (\mathbf{A}^H(\theta_i) \mathbf{A}(\theta_j) + \mathbf{A}^H(\theta_j) \mathbf{A}(\theta_i)) \Phi_l, \tag{45}$$

we can express equation (42) as follows

$$\begin{aligned}
\nabla_{\Phi_l} \mathcal{M}^{\text{sense}}(\Phi) &= \frac{g_0(\Phi) - \sum_{i=1}^Q g_i(\Phi)}{1 + \frac{\nu_0}{\sigma_r^2} \|\boldsymbol{\mu}_0\|^2 - \frac{\nu_0}{\sigma_r^2} \sum_{i=1}^Q \frac{\nu_i \boldsymbol{\mu}_0^H \boldsymbol{\mu}_i}{\sigma_r^2 + \nu_i \|\boldsymbol{\mu}_i\|^2}}. \tag{46}
\end{aligned}$$

where $g_i = g_i^{(1)} + g_i^{(2)}$ and

$$g_0(\Phi) = \frac{2\nu_0}{\sigma_r^2} \mathbf{A}^H(\theta_0) \mathbf{A}(\theta_0) \Phi_l, \tag{47}$$

$$g_i^{(1)}(\Phi) = \frac{2\nu_i \Re[\boldsymbol{\mu}_0^H \boldsymbol{\mu}_i]}{(\sigma_r^2 + \nu_i \|\boldsymbol{\mu}_i\|^2)} (\mathbf{A}^H(\theta_0) \mathbf{A}(\theta_i) + \mathbf{A}^H(\theta_i) \mathbf{A}(\theta_0)) \Phi_l, \tag{48}$$

$$g_i^{(2)}(\Phi) = -\frac{2\nu_i^2 |\boldsymbol{\mu}_0^H \boldsymbol{\mu}_i|^2}{(\sigma_r^2 + \nu_i \|\boldsymbol{\mu}_i\|^2)^2} \mathbf{A}^H(\theta_i) \mathbf{A}(\theta_i) \Phi_l. \tag{49}$$

APPENDIX E

PROOF OF THEOREM 1

Before demonstrating the proof, we introduce the following real-valued vectorial notation for compactness. We first denote

$f(\boldsymbol{\phi}) = -\mathcal{M}^{\text{ISAC}}(\Phi)$, where $\boldsymbol{\phi} = \text{vec}(\Phi)$. As a result, we can reformulate projected gradient descent as follows

$$\nabla f(\boldsymbol{\phi}) = - \begin{bmatrix} \text{Re}(\text{vec}(\nabla \mathcal{M}^{\text{ISAC}}(\Phi))) \\ \text{Im}(\text{vec}(\nabla \mathcal{M}^{\text{ISAC}}(\Phi))) \end{bmatrix}. \tag{50}$$

The update equations are now simply represented as

$$\mathbf{z}_{t+1} = \boldsymbol{\phi}_t - \gamma \nabla f(\boldsymbol{\phi}_t), \tag{51}$$

where $\boldsymbol{\phi}_{t+1}$ is further vectorized as follows

$$\boldsymbol{\phi}_{t+1} \triangleq \bar{\boldsymbol{\pi}}(\mathbf{Z}_{t+1}) = - \begin{bmatrix} \text{Re}(\text{vec}(\boldsymbol{\pi}(\mathbf{Z}_{t+1}))) \\ \text{Im}(\text{vec}(\boldsymbol{\pi}(\mathbf{Z}_{t+1}))) \end{bmatrix}. \tag{52}$$

Using the RSS condition in **Definition 1**, and exploiting (24) for $\mathbf{x}_1 = \boldsymbol{\phi}_t$ and $\mathbf{x}_2 = \boldsymbol{\phi}_{t+1}$, we have the following series of (in)equalities that hold true for all $\boldsymbol{\phi}_t, \boldsymbol{\phi}_{t+1}$, namely

$$\begin{aligned}
\Delta_{t+1} &\stackrel{(a)}{\leq} \nabla f^T(\boldsymbol{\phi}_t) (\boldsymbol{\phi}_{t+1} - \boldsymbol{\phi}_t) + \frac{\beta}{2} \|\boldsymbol{\phi}_t - \boldsymbol{\phi}_{t+1}\|^2 + \frac{\alpha}{2} \epsilon^2 \\
&\stackrel{(b)}{=} \frac{1}{\gamma} (\boldsymbol{\phi}_t - \mathbf{z}_{t+1})^T (\boldsymbol{\phi}_{t+1} - \boldsymbol{\phi}_t) + \frac{\beta}{2} \|\boldsymbol{\phi}_t - \boldsymbol{\phi}_{t+1}\|^2 + \frac{\alpha}{2} \epsilon^2 \\
&\stackrel{(c)}{=} \frac{\beta}{2} (\|\boldsymbol{\phi}_{t+1} - \mathbf{z}_{t+1}\|^2 - \|\boldsymbol{\phi}_t - \mathbf{z}_{t+1}\|^2) + \frac{\alpha}{2} \epsilon^2 \\
&\stackrel{(d)}{\leq} \frac{\beta}{2} (\|\boldsymbol{\phi}^{\text{opt}} - \mathbf{z}_{t+1}\|^2 - \|\boldsymbol{\phi}_t - \mathbf{z}_{t+1}\|^2) + \frac{\alpha}{2} \epsilon^2 \\
&\stackrel{(e)}{=} \frac{\beta}{2} (\|\boldsymbol{\phi}^{\text{opt}} - \boldsymbol{\phi}_t\|^2 + 2(\boldsymbol{\phi}^{\text{opt}} - \boldsymbol{\phi}_t)^T (\boldsymbol{\phi}_t - \mathbf{z}_{t+1})) + \frac{\alpha}{2} \epsilon^2 \\
&\stackrel{(f)}{=} \frac{\beta}{2} \|\boldsymbol{\phi}^{\text{opt}} - \boldsymbol{\phi}_t\|^2 + (\boldsymbol{\phi}^{\text{opt}} - \boldsymbol{\phi}_t)^T \nabla f(\boldsymbol{\phi}_t) + \frac{\alpha}{2} \epsilon^2, \tag{53}
\end{aligned}$$

where $\Delta_{t+1} = f(\boldsymbol{\phi}_{t+1}) - f(\boldsymbol{\phi}_t)$ is the drift in cost at iteration $t+1$ of the projected gradient descent algorithm. In step (a), we utilized the **Definition 1** at $\boldsymbol{\phi}_t, \boldsymbol{\phi}_{t+1}$. In step (b), we used (51). In step (c), we used a descent step size of $\gamma = \frac{1}{\beta}$ and the identity

$$(\mathbf{a} - \mathbf{b})^T (\mathbf{b} - \mathbf{c}) = \frac{1}{2} (\|\mathbf{a} - \mathbf{c}\|^2 - \|\mathbf{a} - \mathbf{b}\|^2 - \|\mathbf{b} - \mathbf{c}\|^2), \tag{54}$$

for any real-valued p -dimensional vectors, $\mathbf{a}, \mathbf{b}, \mathbf{c}$. In step (d), we have used the property that for all $\mathbf{x} = \bar{\boldsymbol{\pi}}(\mathbf{X})$, such that $\mathbf{X} \in \text{St}(L, N_t)$, we have that $\|\boldsymbol{\phi} - \mathbf{z}\|^2 \leq \|\mathbf{x} - \mathbf{z}\|^2$, for $\boldsymbol{\phi} = \bar{\boldsymbol{\pi}}(\mathbf{z})$ and $\bar{\boldsymbol{\pi}}(\cdot)$ is defined in (52). This property is trivial, as $\boldsymbol{\phi}$ minimizes the distance in criterion (22) on the Stiefel manifold. In step (e), we again apply identity (54). In step (f), we used (51).

Now we leverage the RSC condition given in **Definition 2**. This is done by applying (25) twice. The first time through $\mathbf{x}_2 = \boldsymbol{\phi}^{\text{opt}}$ and $\mathbf{x}_1 = \boldsymbol{\phi}_t$, which gives

$$f(\boldsymbol{\phi}^{\text{opt}}) - f(\boldsymbol{\phi}_t) \geq \nabla f^T(\boldsymbol{\phi}_t) (\boldsymbol{\phi}^{\text{opt}} - \boldsymbol{\phi}_t) + \frac{\alpha}{2} \|\boldsymbol{\phi}_t - \boldsymbol{\phi}^{\text{opt}}\|^2 - \frac{\alpha}{2} \epsilon^2, \tag{55}$$

and the second through $\mathbf{x}_2 = \boldsymbol{\phi}_t$ and $\mathbf{x}_1 = \boldsymbol{\phi}^{\text{opt}}$, i.e.

$$f(\boldsymbol{\phi}_t) - f(\boldsymbol{\phi}^{\text{opt}}) \geq \frac{\alpha}{2} \|\boldsymbol{\phi}_t - \boldsymbol{\phi}^{\text{opt}}\|^2 - \frac{\alpha}{2} \epsilon^2. \tag{56}$$

where in $\nabla f(\boldsymbol{\phi}^{\text{opt}}) = \mathbf{0}$, since the gradient is null at the optimal pilot matrix. Now, multiplying inequality (56) by $\frac{\beta}{\alpha}$ then adding it with inequality (55) gives

$$\begin{aligned}
(1 - \frac{\beta}{\alpha}) (f(\boldsymbol{\phi}^{\text{opt}}) - f(\boldsymbol{\phi}_t)) &\geq \frac{\beta}{2} \|\boldsymbol{\phi}^{\text{opt}} - \boldsymbol{\phi}_t\|^2 \\
&\quad + (\boldsymbol{\phi}^{\text{opt}} - \boldsymbol{\phi}_t)^T \nabla f(\boldsymbol{\phi}_t) - (\alpha + \beta) \frac{\epsilon^2}{2}. \tag{57}
\end{aligned}$$

In (57), we have further relaxed the lower bound by removing the non-negative term, $\frac{\alpha}{2} \|\boldsymbol{\phi}_t - \boldsymbol{\phi}^{\text{opt}}\|^2$. Combining (53) with

(57) gives

$$(1 - \frac{\beta}{\alpha})(f(\boldsymbol{\phi}^{\text{opt}}) - f(\boldsymbol{\phi}_t)) \geq -(\alpha + \frac{\beta}{2})\epsilon^2 + \Delta_{t+1}. \quad (58)$$

Then, by adding and subtracting the term $f(\boldsymbol{\phi}^{\text{opt}})$ on the lower bound in (58) gives

$$\frac{\beta}{\alpha}(f(\boldsymbol{\phi}_t) - f(\boldsymbol{\phi}^{\text{opt}})) + (\alpha + \frac{\beta}{2})\epsilon^2 \geq f(\boldsymbol{\phi}_{t+1}) - f(\boldsymbol{\phi}^{\text{opt}}). \quad (59)$$

Applying (59) over t iterations enables us to bound $f(\boldsymbol{\phi}_{t+1}) - f(\boldsymbol{\phi}^{\text{opt}})$ as follows

$$\begin{aligned} f(\boldsymbol{\phi}_{t+1}) - f(\boldsymbol{\phi}^{\text{opt}}) &\leq (\frac{\beta}{\alpha})^{t+1}[f(\boldsymbol{\phi}_0) - f(\boldsymbol{\phi}^{\text{opt}})] \\ &\quad + (\alpha + \frac{\beta}{2})\epsilon^2 \sum_{k=0}^t (\frac{\beta}{\alpha})^k, \end{aligned} \quad (60)$$

where by applying geometric progression, i.e. $\sum_{k=0}^n aq^k = \frac{a(q^{n+1}-1)}{q-1}$ [56], we get

$$\begin{aligned} f(\boldsymbol{\phi}_{t+1}) - f(\boldsymbol{\phi}^{\text{opt}}) &\leq (\frac{\beta}{\alpha})^{t+1}(f(\boldsymbol{\phi}_0) - f(\boldsymbol{\phi}^{\text{opt}})) \\ &\quad + (\alpha + \frac{\beta}{2})\epsilon^2 \frac{1 - (\frac{\beta}{\alpha})^{t+1}}{1 - \frac{\beta}{\alpha}}. \end{aligned} \quad (61)$$

Provided that $\frac{\beta}{\alpha} < 1$, it is easily observed that as $t \rightarrow \infty$, we have that

$$f(\boldsymbol{\phi}_\infty) - f(\boldsymbol{\phi}^{\text{opt}}) \leq (\alpha + \frac{\beta}{2})\epsilon^2 \frac{1}{1 - \frac{\beta}{\alpha}}. \quad (62)$$

Replacing $f(\boldsymbol{\phi})$ with $-\mathcal{M}^{\text{ISAC}}(\boldsymbol{\Phi})$, we arrive at the result in (26), which finalizes the proof of the theorem.

APPENDIX F PROOF OF THEOREM 2

Herein, we lower bound the adopted MI communication metric as follows,

$$\begin{aligned} \mathcal{M}_k^{\text{comm}}(\boldsymbol{\Phi}) &\stackrel{(a)}{\geq} I(\hat{\mathbf{h}}_k; \mathbf{h}_k | \boldsymbol{\Phi}) \\ &\stackrel{(b)}{=} h(\mathbf{h}_k | \boldsymbol{\Phi}) - h(\mathbf{h}_k | \hat{\mathbf{h}}_k, \boldsymbol{\Phi}) \\ &\stackrel{(c)}{=} h(\mathbf{h}_k | \boldsymbol{\Phi}) - h(\tilde{\mathbf{h}}_k | \hat{\mathbf{h}}_k, \boldsymbol{\Phi}) \\ &\stackrel{(d)}{\geq} h(\mathbf{h}_k | \boldsymbol{\Phi}) - h(\tilde{\mathbf{h}}_k | \boldsymbol{\Phi}) \\ &\stackrel{(e)}{\geq} h(\mathbf{h}_k | \boldsymbol{\Phi}) - \log \left(\det \left(\pi e \mathbf{R}_{\tilde{\mathbf{h}}_k} \right) \right) \\ &\stackrel{(f)}{\geq} h(\mathbf{h}_k | \boldsymbol{\Phi}) - N_t \log(\pi e) - N_t \log \frac{\text{tr}(\mathbf{R}_{\tilde{\mathbf{h}}_k})}{N_t}. \end{aligned} \quad (63)$$

In the above series of steps, step (a) follows by the data processing inequality by the following Markov chain $\mathbf{h}_k \rightarrow \mathbf{y}_k \rightarrow \hat{\mathbf{h}}_k$ [39]. Step (b) applies the definition of mutual information as function of entropy h [39]. Step (c) exploits the fact that adding/subtracting a conditioned quantity does not alter entropy and introduces the estimation error vector $\tilde{\mathbf{h}}_k = \mathbf{h}_k - \hat{\mathbf{h}}_k$. Step (d) leverages the fact that conditioning decreases uncertainty, hence increases entropy. Step (e) lower bounds the mutual information using the MSE matrix, i.e. $\mathbf{R}_{\tilde{\mathbf{h}}_k} = \mathbb{E}[\tilde{\mathbf{h}}_k \tilde{\mathbf{h}}_k^H]$, by using the fact that the entropy on a Gaussian distributed random variable maximizes entropy [39]. Step (f) follows by applying the arithmetic mean-geometric mean inequality on positive semidefinite matrices, namely $\frac{\text{tr}(\mathbf{X})}{N} \geq (\det(\mathbf{X}))^{\frac{1}{N}}$ where $\mathbf{X} \succeq \mathbf{0}$ is $N \times N$.

APPENDIX G PROOF OF THEOREM 3

For the hypothesis testing problem in (16), we can define the corresponding probability densities per hypothesis as

$$\begin{aligned} f(\mathbf{z} | \mathcal{H}_0) &\propto \frac{1}{|\mathbf{I}|} e^{-\mathbf{z}^H \mathbf{I}^{-1} \mathbf{z}}, \\ f(\mathbf{z} | \mathcal{H}_1) &\propto \frac{1}{|\mathbf{I} + \mathbf{A}|} e^{-\mathbf{z}^H (\mathbf{I} + \mathbf{A})^{-1} \mathbf{z}}, \end{aligned} \quad (64)$$

where $\mathbf{A} = (\mathbf{R}_{\text{cc}} + \sigma_r^2 \mathbf{I})^{-\frac{1}{2}} \mathbf{R}_{\text{dd}} (\mathbf{R}_{\text{cc}} + \sigma_r^2 \mathbf{I})^{-\frac{1}{2}}$. Stein's lemma states that for a fixed probability of false alarm, we have that

$$\mathcal{D}(f(\mathbf{z} | \mathcal{H}_0) \| f(\mathbf{z} | \mathcal{H}_1)) = \lim_{L \rightarrow \infty} \left(-\frac{1}{L} \log(1 - P_D) \right).$$

The Kullback-Leibler (KL)-divergence is given as [57]

$$\mathcal{D}(p_0 \| p_1) = \mathbb{E}_{p_0} \left[\ln \left[\frac{p_0(\mathbf{z})}{p_1(\mathbf{z})} \right] \right]. \quad (65)$$

It is worth noting that the divergence is also referred to as the power exponent of the most powerful test, i.e. the likelihood ratio test according to Neyman-Pearson lemma [58]. Note that the power exponent can be expressed as

$$\begin{aligned} &\mathcal{D}(f(\mathbf{z} | \mathcal{H}_0) \| f(\mathbf{z} | \mathcal{H}_1)) \\ &\stackrel{(a)}{=} \mathbb{E}_{p_0} \left[\ln \left[\frac{|\mathbf{I} + \mathbf{A}|}{|\mathbf{I}|} e^{-\mathbf{z}^H (\mathbf{I}^{-1} - (\mathbf{I} + \mathbf{A})^{-1}) \mathbf{z}} \right] \right] \\ &\stackrel{(b)}{=} \mathbb{E}_{p_0} \left[\ln \frac{|\mathbf{I} + \mathbf{A}|}{|\mathbf{I}|} - \mathbf{z}^H (\mathbf{I} - (\mathbf{I} + \mathbf{A})^{-1}) \mathbf{z} \right] \\ &\stackrel{(c)}{=} \mathbb{E}_{p_0} \left[\ln \frac{|\mathbf{I} + \mathbf{A}|}{|\mathbf{I}|} \right] - \mathbb{E}_{p_0} [\mathbf{z}^H (\mathbf{I} - (\mathbf{I} + \mathbf{A})^{-1}) \mathbf{z}] \\ &\stackrel{(d)}{=} \ln \frac{|\mathbf{I} + \mathbf{A}|}{|\mathbf{I}|} - \text{Tr}(\mathbf{I} - (\mathbf{I} + \mathbf{A})^{-1}) \\ &\stackrel{(e)}{=} \mathcal{M}^{\text{sense}}(\boldsymbol{\Phi}) - \frac{\nu_0 \boldsymbol{\mu}_0^H \left(\sum_{i=1}^Q \nu_i \boldsymbol{\mu}_i \boldsymbol{\mu}_i^H + \sigma_r^2 \mathbf{I} \right)^{-1} \boldsymbol{\mu}_0}{1 + \nu_0 \boldsymbol{\mu}_0^H \left(\sum_{i=1}^Q \nu_i \boldsymbol{\mu}_i \boldsymbol{\mu}_i^H + \sigma_r^2 \mathbf{I} \right)^{-1} \boldsymbol{\mu}_0}. \end{aligned} \quad (66)$$

In the above series of steps, step (a) applies the definition of KL-divergence. Step (b) applies the logarithm. Step (c) invokes the linearity of the expectation operator. Step (d) applies the expectation on both terms, where the first term is deterministic and the second term uses the fact that for a complex standard Gaussian vector (which is the distribution of \mathbf{z} under \mathcal{H}_0), the quadratic expectation is $\mathbb{E}_{p_0} [\mathbf{z}^H \mathbf{M} \mathbf{z}] = \text{Tr}(\mathbf{M})$. Step (e) uses the definition of $\mathcal{M}^{\text{sense}}(\boldsymbol{\Phi})$ (equation (40)) on the first term, along with the Sherman-Morrison formula applied on the second term.

REFERENCES

- [1] M. Chafii *et al.*, "Twelve Scientific Challenges for 6G: Rethinking the Foundations of Communications Theory," *IEEE Communications Surveys & Tutorials*, vol. 25, no. 2, pp. 868–904, 2023.
- [2] A. Liu *et al.*, "A Survey on Fundamental Limits of Integrated Sensing and Communication," *IEEE Communications Surveys & Tutorials*, vol. 24, no. 2, pp. 994–1034, 2022.
- [3] J. A. Zhang *et al.*, "Enabling Joint Communication and Radar Sensing in Mobile Networks—A Survey," *IEEE Communications Surveys & Tutorials*, vol. 24, no. 1, pp. 306–345, 2022.
- [4] —, "An Overview of Signal Processing Techniques for Joint Communication and Radar Sensing," *IEEE Journal of Selected Topics in Signal Processing*, vol. 15, no. 6, pp. 1295–1315, 2021.
- [5] U. Demirhan and A. Alkhateeb, "Integrated Sensing and Communication for 6G: Ten Key Machine Learning Roles," *IEEE Communications Magazine*, vol. 61, no. 5, pp. 113–119, 2023.
- [6] Y. L. Sit *et al.*, "2D radar imaging with velocity estimation using

- a MIMO OFDM-based radar for automotive applications,” in *2013 European Radar Conference*. IEEE, 2013, pp. 145–148.
- [7] L. Zheng *et al.*, “Radar and communication coexistence: An overview: A review of recent methods,” *IEEE Signal Processing Magazine*, vol. 36, no. 5, pp. 85–99, 2019.
 - [8] A. Hassaniien *et al.*, “Dual-Function Radar Communication Systems: A Solution to the Spectrum Congestion Problem,” *IEEE Signal Processing Magazine*, vol. 36, no. 5, pp. 115–126, 2019.
 - [9] C. Shi *et al.*, “Power Minimization-Based Robust OFDM Radar Waveform Design for Radar and Communication Systems in Coexistence,” *IEEE Trans. Signal Process.*, vol. 66, no. 5, pp. 1316–1330, 2018.
 - [10] S. Sodagari, A. Khawar, T. C. Clancy, and R. McGwier, “A projection based approach for radar and telecommunication systems coexistence,” in *2012 IEEE Global Communications Conference (GLOBECOM)*, 2012, pp. 5010–5014.
 - [11] Y. Xiong *et al.*, “On the Fundamental Tradeoff of Integrated Sensing and Communications Under Gaussian Channels,” *IEEE Transactions on Information Theory*, pp. 1–1, 2023.
 - [12] A. Bazzi and M. Chafii, “On Integrated Sensing and Communication Waveforms with Tunable PAPR,” *IEEE Trans. Wireless Commun.*, pp. 1–1, 2023.
 - [13] Z. Xiao and Y. Zeng, “Waveform Design and Performance Analysis for Full-Duplex Integrated Sensing and Communication,” *IEEE J. Sel. Areas in Commun.*, vol. 40, no. 6, pp. 1823–1837, 2022.
 - [14] R. Zhang *et al.*, “Integrated Sensing and Communication Waveform Design With Sparse Vector Coding: Low Sidelobes and Ultra Reliability,” *IEEE Trans. Veh. Technol.*, vol. 71, no. 4, pp. 4489–4494, 2022.
 - [15] F. Liu, Y. Zhang, Y. Xiong, S. Li, W. Yuan, F. Gao, S. Jin, and G. Caire, “OFDM achieves the lowest ranging sidelobe under random ISAC signaling,” *arXiv preprint arXiv:2407.06691*, 2024.
 - [16] A. Bazzi and M. Chafii, “On Outage-based Beamforming Design for Dual-Functional Radar-Communication 6G Systems,” *IEEE Trans. Wireless Commun.*, pp. 1–1, 2023.
 - [17] J. Wu, Z. Wang, Y.-F. Liu, and F. Liu, “Efficient Global Algorithms for Transmit Beamforming Design in ISAC Systems,” *IEEE Transactions on Signal Processing*, 2024.
 - [18] Q. Qi *et al.*, “Integrated Sensing, Computation and Communication in B5G Cellular Internet of Things,” *IEEE Trans. Wireless Commun.*, vol. 20, no. 1, pp. 332–344, 2021.
 - [19] Z. Lyu *et al.*, “Joint Maneuver and Beamforming Design for UAV-Enabled Integrated Sensing and Communication,” *IEEE Trans. Wireless Commun.*, vol. 22, no. 4, pp. 2424–2440, 2023.
 - [20] Z. Xiao and Y. Zeng, “Integrated Sensing and Communication with Delay Alignment Modulation: Performance Analysis and Beamforming Optimization,” *IEEE Trans. Wireless Commun.*, pp. 1–1, 2023.
 - [21] J. Mu *et al.*, “Integrated Sensing and Communication-Enabled Predictive Beamforming With Deep Learning in Vehicular Networks,” *IEEE Comm. Letters*, vol. 25, no. 10, pp. 3301–3304, 2021.
 - [22] J. An *et al.*, “Fundamental Detection Probability vs. Achievable Rate Tradeoff in Integrated Sensing and Communication Systems,” *IEEE Trans. Wireless Commun.*, pp. 1–1, 2023.
 - [23] H. Zhang *et al.*, “Holographic Integrated Sensing and Communication,” *IEEE J. Sel. Areas in Commun.*, vol. 40, no. 7, pp. 2114–2130, 2022.
 - [24] Z. Gao *et al.*, “Integrated Sensing and Communication With mmWave Massive MIMO: A Compressed Sampling Perspective,” *IEEE Trans. Wireless Commun.*, vol. 22, no. 3, pp. 1745–1762, 2023.
 - [25] A. Bazzi and M. Chafii, “RIS-Enabled Passive Radar towards Target Localization,” *arXiv preprint arXiv:2210.11887*, 2022.
 - [26] Z. Wang *et al.*, “STARS Enabled Integrated Sensing and Communications,” *IEEE Trans. Wireless Commun.*, pp. 1–1, 2023.
 - [27] Y. Wu *et al.*, “Sensing Integrated DFT-Spread OFDM Waveform and Deep Learning-Powered Receiver Design for Terahertz Integrated Sensing and Communication Systems,” *IEEE Trans. Commun.*, vol. 71, no. 1, pp. 595–610, 2023.
 - [28] B. Li *et al.*, “A Distributionally Robust Linear Receiver Design for Multi-Access Space-Time Block Coded MIMO Systems,” *IEEE Trans. Wireless Commun.*, vol. 16, no. 1, pp. 464–474, 2017.
 - [29] V. Ntranos *et al.*, “On multicast beamforming for minimum outage,” *IEEE Trans. Wireless Commun.*, vol. 8, no. 6, pp. 3172–3181, 2009.
 - [30] Y. Gu *et al.*, “Radar Target Profiling and Recognition Based on TSI-Optimized Compressive Sensing Kernel,” *IEEE Trans. Signal Process.*, vol. 62, no. 12, pp. 3194–3207, 2014.
 - [31] J. Li, L. Xu, P. Stoica, K. W. Forsythe, and D. W. Bliss, “Range Compression and Waveform Optimization for MIMO Radar: A Cramér–Rao Bound Based Study,” *IEEE Transactions on Signal Processing*, vol. 56, no. 1, pp. 218–232, 2008.
 - [32] F. Zhang *et al.*, “Joint Range and Velocity Estimation With Intrapulse and Inter-subcarrier Doppler Effects for OFDM-Based RadCom Systems,” *IEEE Trans. Signal Process.*, vol. 68, pp. 662–675, 2020.
 - [33] K. V. Mishra *et al.*, “Toward Millimeter-Wave Joint Radar Communications: A Signal Processing Perspective,” *IEEE Signal Processing Magazine*, vol. 36, no. 5, pp. 100–114, 2019.
 - [34] F. Yin *et al.*, “Parametric Waveform Design Using Discrete Prolate Spheroidal Sequences for Enhanced Detection of Extended Targets,” *IEEE Trans. Signal Process.*, vol. 60, no. 9, pp. 4525–4536, 2012.
 - [35] S. Kay, “Optimal Signal Design for Detection of Gaussian Point Targets in Stationary Gaussian Clutter/Reverberation,” *IEEE Journal of Selected Topics in Signal Processing*, vol. 1, no. 1, pp. 31–41, 2007.
 - [36] 3GPP, “Feasibility Study on Integrated Sensing and Communication (Release 19),” 3rd Generation Partnership Project (3GPP), Tech. Rep. TR 22.837, 2023, available online: <https://www.3gpp.org>.
 - [37] T. Routenberg and J. Tabrikian, “Blind Source Separation for MIMO-AR Mixtures Using GMM,” in *2006 IEEE 24th Convention of Electrical & Electronics Engineers in Israel*, 2006, pp. 310–314.
 - [38] T. T. Nguyen, H. D. Nguyen, F. Chamroukhi, and G. J. McLachlan, “Approximation by finite mixtures of continuous density functions that vanish at infinity,” *Cogent Mathematics & Statistics*, vol. 7, no. 1, p. 1750861, 2020.
 - [39] T. M. Cover, *Elements of Information Theory*. John Wiley & Sons, 1999.
 - [40] M. Bell, “Information theory and radar waveform design,” *IEEE Transactions on Information Theory*, vol. 39, no. 5, pp. 1578–1597, 1993.
 - [41] E. Bjornson, E. A. Jorswieck, M. Debbah, and B. Ottersten, “Multiobjective Signal Processing Optimization: The way to balance conflicting metrics in 5G systems,” *IEEE Signal Processing Magazine*, vol. 31, no. 6, pp. 14–23, 2014.
 - [42] M. Ehrgott, *Multicriteria optimization*. Springer Science & Business Media, 2005, vol. 491.
 - [43] S. P. Boyd and L. Vandenberghe, *Convex optimization*. Cambridge university press, 2004.
 - [44] S. Zhang *et al.*, “A low-overhead energy detection based cooperative sensing protocol for cognitive radio systems,” *IEEE Trans. Wireless Commun.*, vol. 8, no. 11, pp. 5575–5581, 2009.
 - [45] R. F. Barber and W. Ha, “Gradient descent with non-convex constraints: Local Concavity Determines Convergence,” *Information and Inference: A Journal of the IMA*, vol. 7, no. 4, pp. 755–806, 03 2018. [Online]. Available: <https://doi.org/10.1093/imaia/iy002>
 - [46] P.-L. Loh and M. J. Wainwright, “Regularized M-estimators with non-convexity: Statistical and algorithmic theory for local optima,” *Advances in Neural Information Processing Systems*, vol. 26, 2013.
 - [47] B. Hassibi and B. Hochwald, “How much training is needed in multiple-antenna wireless links?” *IEEE Transactions on Information Theory*, vol. 49, no. 4, pp. 951–963, 2003.
 - [48] F. Kanaya and K. Nakagawa, “On the practical implication of mutual information for statistical decisionmaking,” *IEEE Transactions on Information Theory*, vol. 37, no. 4, pp. 1151–1156, 1991.
 - [49] G. Fatima, P. Stoica, A. Aubry, A. De Maio, and P. Babu, “Optimal Placement of the Receivers for Multistatic Target Localization,” *IEEE Transactions on Radar Systems*, vol. 2, pp. 391–403, 2024.
 - [50] S. R. Saunders and A. Aragón-Zavala, *Antennas and propagation for wireless communication systems*. John Wiley & Sons, 2007.
 - [51] S. M. Kay, *Fundamentals of statistical signal processing: estimation theory*. Prentice-Hall, Inc., 1993.
 - [52] D. Guo, S. Shamai, S. Verdú *et al.*, “The interplay between information and estimation measures,” *Foundations and Trends® in Signal Processing*, vol. 6, no. 4, pp. 243–429, 2013.
 - [53] B. Fesl *et al.*, “Channel estimation based on Gaussian mixture models with structured covariances,” *arXiv preprint arXiv:2205.03634*, 2022.
 - [54] S. Bazzi and W. Xu, “Downlink Training Sequence Design for FDD Multiuser Massive MIMO Systems,” *IEEE Transactions on Signal Processing*, vol. 65, no. 18, pp. 4732–4744, 2017.
 - [55] M. Alsabah, M. A. Naser, B. M. Mahmood, N. K. Noordin, and S. H. Abdulhussain, “Sum Rate Maximization Versus MSE Minimization in FDD Massive MIMO Systems With Short Coherence Time,” *IEEE Access*, vol. 9, pp. 108 793–108 808, 2021.
 - [56] I. S. Gradshteyn and I. M. Ryzhik, *Table of integrals, series, and products*. Academic press, 2014.
 - [57] M. J. Borran, A. Sabharwal, and B. Aazhang, “Design criterion and construction methods for partially coherent multiple antenna constellations,” *IEEE Transactions on Wireless Communications*, vol. 8, no. 8, pp. 4122–4133, 2009.
 - [58] L. L. Scharf and C. Demeure, “Statistical signal processing: detection, estimation, and time series analysis,” (*No Title*), 1991.